Titre: Title:	A Wide-Field Raman Imaging Approach for Detection of the CH2/CH3 Deformation Band with System Integration and Preliminary Evaluation
Auteur: Author:	Samaneh Pahlavani
Date:	2025
Type:	Mémoire ou thèse / Dissertation or Thesis
Référence: Citation:	Pahlavani, S. (2025). A Wide-Field Raman Imaging Approach for Detection of the CH2/CH3 Deformation Band with System Integration and Preliminary Evaluation [Mémoire de maîtrise, Polytechnique Montréal]. PolyPublie. https://publications.polymtl.ca/71125/

POLYTECHNIQUE MONTRÉAL
affiliée à l'Université de Montréal

A Wide-Field Raman Imaging Approach for Detection of the CH_2/CH_3 Deformation Band with System Integration and Preliminary Evaluation

SAMANEH PAHLAVANI
Institut de génie biomédical

Mémoire présenté en vue de l'obtention du diplôme de *Maîtrise ès sciences appliquées*

Génie biomédical

Décembre 2025

POLYTECHNIQUE MONTRÉAL
affiliée à l'Université de Montréal

Ce mémoire intitulé :

A Wide-Field Raman Imaging Approach for Detection of the CH_2/CH_3 Deformation Band with System Integration and Preliminary Evaluation

présenté par **Samaneh PAHLAVANI**
en vue de l'obtention du diplôme de *Maîtrise ès sciences appliquées*
a été dûment accepté par le jury d'examen constitué de :

Frédéric LESAGE, président
Frédéric LEBLOND, membre et directeur de recherche
Stephan REUTER, membre

DEDICATION

To my family, whose unwavering love, sacrifices, and quiet strength have carried me through every challenge. Your belief in me, even when I doubted myself, gave me the courage to pursue any journey.

ACKNOWLEDGEMENTS

I would like to express my deepest gratitude to my supervisor, Prof. Frédéric Leblond, for his invaluable guidance, encouragement and support throughout this project. His insights, scientific rigor, and unwavering enthusiasm have been a constant source of motivation and inspiration.

I am also sincerely thankful to the members of the LUMED Laboratory for their collaboration, feedback, and technical support. In particular, I want to thank Sandryn for her guidance and feedback during her presence in the lab, which helped me learn the initial steps. To Guillaume for his scientific and software-related feedback. To Gabriel, for his assistance during ex vivo cases. To Julitte, for her help in smoothing the administration and her gentle care. To Fredo for kindly sharing his feedback about the data processing, and for the cat pictures that make the lab's mood up:) To my colleagues, Trang, Katie, Hugo, Alice, Victor, Frank, Esmat, Nassim, Laurance, Tommy, and Romane. I would like to thank you for creating a supportive and collaborative environment that made every challenge more manageable and every success more meaningful.

Special thanks to the Montreal Neurological Institute (MNI) and Dr. Kevin Petrecca, a well-known neurosurgeon who is passionate about developing new technologies and his collaboration on Raman studies. Marie Josef, for providing access to clinical facilities and samples, and Dr. Marie-Christine Guiot for interpreting the pathology results.

The author acknowledges the use of ChatGPT (OpenAI, August 2025 version) as a writing assistant to improve the clarity of certain sections. All content has been verified and is the sole responsibility of the author.

RÉSUMÉ

Chaque jour au Canada, 27 personnes reçoivent un diagnostic de tumeur cérébrale primitive, et seulement 25% des patients atteints de tumeurs cérébrales malignes survivent cinq ans ou plus [1]. La résection chirurgicale demeure le traitement principal des cancers du cerveau. Cependant, la présence de tissu ou de cellules cancéreuses résiduelles peut entraîner des récidives. Les patients présentant une marge chirurgicale positive ont un risque de progression du cancer 3,7 fois plus élevé que ceux ayant une marge négative [2–4]. En éliminant les cellules résiduelles, le risque de récidive peut être réduit, ce qui conduit à de meilleurs résultats pour les patients et à une survie prolongée [5].

De plus, une résection trop étendue dans les tissus sains peut nuire à la qualité de vie des patients atteints de tumeurs cérébrales en affectant des zones clés du cerveau. Malgré des avancées significatives dans les technologies et les techniques chirurgicales [6–9], les taux de résection complète demeurent inférieurs à 10–20 %. Le besoin de reprises chirurgicales persiste non seulement pour les cancers du cerveau [10–12], mais aussi pour d'autres types de cancers, notamment le cancer du sein [12] et de la prostate [13]. La spectroscopie Raman est une technologie basée sur un laser pouvant guider les chirurgiens à détecter l'étendue complète des tumeurs cancéreuses durant la chirurgie, tout en évitant les tissus cérébraux sains. La spectroscopie Raman spontanée, sans marqueur (RS), permet de révéler des informations biomoléculaires sous forme d'empreinte spectrale des tissus. Une lumière est dirigée sur un échantillon, et la lumière rétrodiffusée de manière inélastique (Raman) contient une empreinte biomoléculaire détectée par un spectromètre Raman. Cette empreinte peut ensuite être comparée à une base de données de référence histologique à l'aide de méthodes d'apprentissage automatique, pour générer des modèles prédictifs [14, 15].

Dans ce projet, je développerai un système rapide à champ large avec un champ de vision de 2 cm^2, une résolution spatiale de 250 μm et une résolution spectrale de 6 cm^{-1}. Cela sera rendu possible grâce aux recherches récentes effectuées dans notre laboratoire, qui ont introduit une nouvelle technique de détection de diffusion inélastique appelée spectroscopie Raman macroscopique multispectrale (MSRS) [16]. Le projet se concentrera sur les bandes ciblées CH_2/CH_3 autour de 1440 cm^{-1}. Notre laboratoire a identifié cette bande comme biomarqueur du cancer, fournissant des informations métaboliques sur le rapport relatif entre protéines et lipides [17].

ABSTRACT

Every day in Canada, 27 people are diagnosed with primary brain tumors, and only 25% of malignant brain tumor patients survive for 5 years or more [1]. Surgical resection remains the primary treatment for brain cancer. However, the presence of residual cancer tissue and cells can cause recurrence. Patients with a positive surgical margin have a 3.7x higher risk of cancer progression than those with a negative surgical margin [2–4]. By removing residual cells, the risk of cancer recurrence can be lowered, ultimately leading to improved patient outcomes and increased survival [5]. Furthermore, resecting too far into healthy tissue can negatively affect the quality of life of brain tumor patients by impacting key parts of the brain. Despite significant advances in surgical technology and techniques [6–9], the rates of complete resection remain below 10-20%. The need for re-excision persists for not only brain cancer [10–12] but also other cancer types, including breast [12] and prostate [13]. Raman spectroscopy is a laser-based technology that can guide surgeons in detecting the full extent of cancerous tumors during surgery while avoiding healthy brain tissue. Label-free spontaneous Raman spectroscopy (RS) can reveal biomolecular information in the form of tissue spectral fingerprints. Light is shone on a sample, and the light inelastically (Raman) scattered back from the sample contains a biomolecular fingerprint, which is detected using a Raman spectrometer. This biomolecular fingerprint can be matched with a known reference set by histology using machine learning methods, resulting in predictive mathematical models [14,15]. In this project, I will develop a rapid, wide-field system with a 2 cm^2 field of view, with a spatial resolution of 250 μ m and a spectral resolution of 6 cm^{-1} This will be achieved based on the latest research conducted in our laboratory, which introduced a new inelastic scattering detection technique called macroscopic multi-spectral Raman spectroscopy (MSRS) [16]. The focus of the project will be on the targeted bands at CH_2/CH_3 at approximately 1440 cm^{-1}. Our lab has indicated this band as a cancer biomarker that provides metabolic information relating to the relative ratio of proteins and lipids [17].

TABLE OF CONTENTS

DEDICATION iii

ACKNOWLEDGEMENTS iv

RÉSUMÉ v

ABSTRACT vi

LIST OF TABLES x

LIST OF FIGURES xi

LIST OF SYMBOLS AND ACRONYMS xvi

CHAPTER 1 INTRODUCTION 1
1.1 Clinical Motivation 1
1.1.1 Intraoperative MRI (iMRI) 3
1.1.2 5-Aminolevulinic Acid (5-ALA) Fluorescence Guidance 4
1.1.3 Intraoperative Ultrasound (IOUS) 6
1.1.4 Histopathology Analysis 8
1.2 Research Hypotheses 10
1.3 Research Objectives 10
1.3.1 Objective 1: Automate Signal Acquisition and Control 10
1.3.2 Objective 2: To repackage and Integrate the System into a Standalone Clinical Unit 11
1.3.3 Objective 3: To Assess System Performance Using Porcine/Muscle tissues 11
1.3.4 Objective 4: Clinical Evaluation During Pilot Study 11
1.4 Thesis Organization 12

CHAPTER 2 LITERATURE REVIEW 13
2.1 Light–Matter Interactions 13
2.1.1 Fluorescence 13
2.1.2 Absorption 13
2.1.3 Reflection and Refraction 16
2.1.4 Scattering 17
2.2 Raman Spectroscopy and Imaging Systems 19

2.2.1 Imaging Configurations 20
2.3 Raman in Neurosurgical Applications 21
2.3.1 Raman Probes 21
2.3.2 Wide-Field Raman Imaging Systems 22
2.4 Limitations in Current Technologies 25

CHAPTER 3 SYSTEM DESIGN AND DEVELOPMENT 27
3.1 Optical Design and Components 27
3.1.1 Laser Illumination Source 27
3.1.2 CCD Camera: Andor iKon-M 934 28
3.1.3 Filter Wheel: FLI High Speed Filter Wheel 29
3.2 Hardware-Software Synchronization 30
3.2.1 Automation and Control of Filter Wheel via Python 30
3.2.2 Collection and Detection Path 32
3.2.3 Illumination Path 32
3.3 Spectral and Spatial Resolution Characterization 33
3.3.1 Spatial Resolution Measurement Using USAF Target 33
3.3.2 Spectral Resolution 34
3.4 Noise Sources and Mitigation Strategies 34
3.4.1 Readout and Electronic Noise 35
3.4.2 Dark Current and Thermal Noise 35
3.4.3 Photon Shot Noise 35
3.4.4 Interference Effects: Scattering Artifacts and Etaloning 35
3.4.5 Environmental and Systemic Noise 36
3.4.6 SNR System Sensitivity 36

CHAPTER 4 PRECLINICAL EVALUATION 38
4.1 Chapter Overview 38
4.2 Sample Preparation and Acquisition Protocol 38
4.2.1 Sample Preparation: Biological Tissue 40
4.2.2 Laser Exposure and Illumination Area 40
4.2.3 Multi-spectral Image Acquisition 40
4.2.4 Diffuse Reflectance Calibration Using Spectralon 40
4.2.5 Spectral Calibration with NIST Standard 41
4.3 Spectral Processing and Baseline Correction 41
4.3.1 Data Organization and Loading 41
4.3.2 Dark Signal Removal 41

4.3.3 Diffuse Reflectance Calibration Using Spectralon 41
4.3.4 Spectral Correction Using NIST Standard 42
4.3.5 Fluorescence Background Subtraction and Baseline Correction 42
4.3.6 Baseline Algorithms Used 42
4.3.7 Raman Band Selection and Correction Schemes 43
4.4 Processed Imaging Results: Fat vs. Muscle 45
4.4.1 Multispectral Raw Raman Images (Preprocessed) 45
4.4.2 Baseline Subtracted Raman Maps at 1440 cm^{-1} 48
4.4.3 Quantitative Comparison 49
4.4.4 Conclusion, and Final Results 50

CHAPTER 5 CLINICAL APPLICATION AND TESTING 51
5.1 Surgical Environment Setup 51
5.2 Specimen Preparation and Histology Alignment 53
5.3 Image acquisition process 54
5.4 Image Processing Steps for brain data 54
5.4.1 ROC Analysis Using Probe Data 58
5.5 Preliminary Clinical Results 60
5.6 Discussion 62
5.6.1 Processing pipeline: where each correction is applied and how 62

CHAPTER 6 DISCUSSION AND CONCLUSION 65
6.1 Summary of Contributions 65
6.2 Advantages of the Proposed Technology 65
6.3 Technical and Clinical Limitations 66
6.4 Future Studies Direction 67
6.4.1 Targeting 1004, 1340, and 1430–1460 cm^{-1} Bands: 67
6.4.2 Precise alignment of Histology and Raman Images and measuring accuracy: 67
6.4.3 Real-time Raman Classification: 68
6.4.4 Multi modal Integration: 68
6.4.5 Power Analysis and Sample Size: 69
6.4.6 Ex vivo Validation Only: 70

REFERENCES 71

LIST OF TABLES

Table 3.1	Key Specifications of the Andor iKon-M 934 Camera	29
Table 3.2	Detection Wavelengths and Spectral Resolution for Filters Used Near 1440 cm^{-1}	34
Table 3.3	System performance summary	37
Table 5.1	Summary of analyzed brain tissue samples used for Raman baseline removal evaluation. Each sample corresponds to a distinct histological case and figure reference in the Results section.	60

LIST OF FIGURES

Figure 1.1 Illustration of common brain tumor types: glioblastoma multiform (infiltration, WHO Grade IV), meningioma (arising from the meninges), and brain metastasis (typically well-circumscribed lesions from systemic cancers). Adapted from the Medical Art Library. 2

Figure 1.2 Figure shows how intraoperative MRI was used to guide the resection of a brain tumor located near critical functional areas. The images before surgery (a, b) highlight the tumor in light blue, along with nearby important regions, such as Wernicke's area (green) and visual pathways (purple and pink). The surgical plan, including the target point and path, was overlaid. During the operation, the neuro navigation system projected this information into the surgeon's microscope view (c), showing both functional areas and major blood vessels. The first round of imaging revealed that some tumor tissue remained (e, red arrows). After updating the navigation system with this new information, the surgery was continued. The adjusted microscope view (d) helped the surgeon focus on the remaining tumor area (outlined in yellow). Final images (f) confirmed that the tumor was completely removed [18]. . . 4

Figure 1.3 Preoperative MRI scans (left) display the tumor location, while postoperative images (right) confirm the extent of resection. The central column presents the surgical cavity. The top image shows the tumor under standard white light illumination, the middle image reveals the fluorescent signal under blue light, highlighting pinkish tones, and the bottom image displays a merged view using multi spectral fluorescence (MFL) mode, where the tumor appears in green pseudo-color. Reprinted from [19] with permission. 6

Figure 1.4 Example showing how a glioblastoma multiform appears in both intraoperative ultrasound and preoperative MRI. In this case, the tumor has a visibility grade of 3 in both the ultrasound image (A) and MRI scan (B), indicating clear and comparable visualization across both modalities. Image reprinted from [20] with permission. 8

Figure 1.5 Comparison of tumor fluorescence and corresponding histology. (a) and (b) show two tumor samples imaged under fluorescence guidance (left) and their matched hematoxylin and eosin (H&E) stained histological sections (right). Fluorescence images highlight the tumor regions, while histology confirms the tissue structure and cellularity. Image reprinted from [21] with permission. 9

Figure 2.1 Jabolonski diagrams for Rayleigh and Raman scattering and Infrared absorption [22]. 19

Figure 2.2 Three primary configurations for Raman macroscopically Imaging [23]. 20

Figure 2.3 The handheld fiber-optic probe for Raman spectroscopy, developed by Emvision, LLC, was utilized to analyze brain tissue during surgical procedures. A schematic diagram on top-left depicting how the probe excites various molecular components, including cholesterol and DNA, to generate Raman spectra distinguishing cancerous tissue from normal brain tissue, as described by Jermyn et al. [24]. 21

Figure 2.4 The experimental workflow for brain tumor detection with the Sentry System includes distinct processes. The blue section highlights the acquisition of spectral fingerprints using a handheld probe during neurosurgical procedures. The red section details the histopathology workflow, where each spectral measurement is matched with the corresponding data, including a pathologist's assessment of the cancer cell burden. Bulk tumor tissue is classified as having more than 90% cancer cell burden, while non-tumor brain tissue is defined by a 0% cancer cell burden. The green section illustrates the Sentry System's application in the real-time classification of tumor versus non-tumor brain tissue [17]. 22

Figure 2.5 Overview of the handheld Raman imaging probe and system schematic. (a) Ergonomic handheld probe integrating illumination and collection optics. (b) The internal configuration includes an excitation fiber bundle (EFB), laser line filter (LLF), mirror (M), and long-pass filter (LPF) for delivering both laser and white light to the tissue for fluorescence excitation. On the collection side, a second LPF, optical window, and notch filter isolate the returning Raman signal, which is transmitted via a collection fiber bundle (CFB). (c) The excitation branch formed a line-shaped laser pattern and injected white light into the EFB mounted on a translation stage (TS). (d) The collection branch separates the white light and Raman signals using a scanning high-pass filter; the white light is directed to an RGB camera for structural imaging, whereas the Raman spectra are acquired using an imaging spectrometer. Spherical lenses are unlabeled, whereas cylindrical lenses are marked with LH (horizontal curvature) or LV (vertical curvature). Adapted from [14, 15] 24

Figure 2.6 Experimental setup enabling multi-spectral detection of inelastic scattering in biological tissues: (a) A schematic diagram illustrating an epi-illumination configuration. The excitation path included an optical fiber, collimating lens (CL), band-pass filter (BPF), diverging lens, dichroic mirror (DM), and focusing lens. The collection path comprises a notch filter (NF), a filter wheel with nine interference band-pass filters, and a CCD camera. (b) A photograph of the system [25]. 25

Figure 3.1 Graphical user interface (GUI) developed for filter wheel (FW) control. The interface allows users to select the device, choose filter positions, adjust the speed, and monitor the connection status and current position in real time. This tool was implemented using PyQt5 and PyVISA to automate filter control within the Raman imaging system. 30

Figure 3.2 Schematic illustration of the wide-field Raman imaging system. The 785 nm laser (right) was fiber-coupled into a collimation package, diverging lens, and laser line filter. The beam was reflected by a dichroic mirror and focused onto the sample through collection lenses. The back-scattered Raman signals pass through the dichroic, notch, band-pass filters in the filter wheel, and detection lenses before reaching the CCD camera. The filter wheel is positioned in the pupil plane between the detection lens pair to enable multi spectral imaging. 33

Figure 4.1 Raman spectra of adipose and muscle tissues captured using the hyperspectral imaging system: (A) Mean raw spectra with corresponding variance across the field of view. (B) Processed spectra following background subtraction, showing reduced variability in the spectra. The vertical dashed lines in (A) indicate the three spectral bands selected for the multi-spectral system, centered at Raman shifts of 1407, 1440, and 1492 cm^{-1}. Reprinted from [25] with permission. 39

Figure 4.2 Spectra of different tissue types; normal, cancer, and fat with the placement of different filter pairs around the 1440 cm^{-1} band. Vertical dashed lines indicate filter centers used for linear interpolation-based baseline correction. 44

Figure 4.3 Raman images captured using five narrow band filters targeting specific Raman shifts around the 1440 cm^{-1} band. Each image represents one acquisition band before baseline subtraction. 45

Figure 4.4 A, B, and C: Images of different filter before correcting by spectralon. D, E, F: Images of the filters after correction by Spectralon. 46

Figure 4.5 Image acquired with the band pass filter at 1440 cm^{-1}, before (left) and after (right) correcting by NIST. 47

Figure 4.6 Baseline-corrected Raman images at 1440 cm^{-1} using different filter pairs for fluorescence estimation. Top left: 1407–1462; top right: 1375–1490; bottom left: 1407–1490; bottom right: 1375–1462. 48

Figure 4.7 Pixel intensity histograms of final Raman Images at 1440 cm^{-1} for different filter Pairs 49

Figure 4.8 Overview of the fat and muscle tissue sample. (a) Mobile phone image of the tissue, (b) Bright-field image showing orientation, (c) Raman intensity distribution at 1440 cm^{-1}, and (d) Tissue classification map distinguishing fat and muscle. 50

Figure 5.1 Experimental setup of the multi-spectral Raman imaging system configured for ex vivo measurements. The system includes a laptop (1) for control, the multi spectral system (2), the laser (3), the black chamber for putting the sample inside (4), and supporting electronics on the lower shelves. 52

Figure 5.2 Step-by-step specimen preparation and histology alignment workflow. This includes tissue collection, PBS immersion, sample trimming, placement on aluminum backing, Raman imaging with PBS spraying to prevent dehydration, inking of tissue borders, cassette transfer, paraformaldehyde fixation, and final H&E staining for histological analysis. 54

Figure 5.3 Mean Raman spectra of glioblastoma (orange, $n = 366$) and normal brain tissue (black, $n = 185$) with standard deviation bands. The top panel shows the overall intensity, including the auto-fluorescence background, while the bottom panel displays the baseline-corrected spectra. A prominent Raman peak near 1440 cm^{-1}, corresponding to CH_2/CH_3 deformations, showed a clear intensity difference between tumor and normal tissue, enabling reliable discrimination. Highlighted region indicates the spectral window of interest for lipid/protein contrast. 56

Figure 5.4 Comparison of baseline subtraction approaches at 1440 cm^{-1}. 58

Figure 5.5 ROC curve for classification between glioblastoma and normal brain tissue based on probe-acquired Raman spectra. 59

Figure 5.6 Comparison of histology(first column), Raman (second column), and reference images (third column) for six samples. 61

LIST OF SYMBOLS AND ACRONYMS

5-ALA	5Aminolevulinic Acid
iMRI	intraoperative Magnetic Resonance Imaging
GBM	Glioblastoma Multiforme
IOUS	Intraoperative Ultrasound
AI	Artificial Intelligence
AR	Anti-Reflective
BF	Bright Field
CCD	Charge-Couple Device
CRCHUM	Centre de Recherche du Centre hospitalier de l'Université de Montréal
CNN	Convolutional Neural Network
FFPE	Formalin Fixation and Paraffin-Embedding
FGS	Fluorescence-Guided Surgery
FOV	Field Of View
H&E	Hematoxylin and Eosin
ML	Machine Learning
MNI	Montreal Neurological Institute and Hospital
MPE	Maximum Permissible Exposure
MSRS	Multi-Spectral Raman Spectroscopy
MUHC	Montreal University Health Centre
NIR	Near-InfraRed
NN	Neural Network
OR	Operating Room
OTF	Optical Transfer Function
QF	Quality Factor
REB	Research Ethics Board
WHO	World Health Organization

CHAPTER 1 INTRODUCTION

1.1 Clinical Motivation

Brain tumor surgery requires precise removal of tissue while preserving the surrounding healthy brain regions that are critical for neurological function. This balance matters because research consistently shows that more complete tumor removal leads to better outcomes across many brain tumor types, including gliomas, meningioma, and brain metastases [26]. But here's the challenge: during surgery, it's often incredibly difficult to tell where the tumor ends and healthy brain begins.

Gliomas are the most common type of malignant brain tumors in adults arising from glia cells that support neurons. They range from relatively slow-growing grade I tumors to aggressive grade IV cancers. Glioblastoma multi forme (GBM), a grade IV astrocytoma, stands out as particularly aggressive. GBMs don't stay put—they infiltrate deep into surrounding brain tissue, making complete removal nearly impossible. Their complex biology includes abnormal cell nuclei, areas of cell death surrounded by tumor cells, and dense blood vessel growth [27]. This complexity makes them resistant to treatment and prone to recurrence even after extensive surgery.

Meningioma, present a different picture. These tumors grow from the protective layers surrounding the brain and are usually benign (grade I). They're actually the most common primary brain tumors and tend to grow slowly. However, some meningioma (grades II and III) behave more aggressively, invading nearby brain or bone and recurring more frequently. Under the microscope, they show distinctive swirling cell patterns and sometimes form small calcified bodies. While often well-defined, their location near critical structures like blood vessels or cranial nerves can complicate removal [17]. Brain metastases are different again—these are cancers that spread to the brain from other parts of the body, most commonly from lung, breast, kidney, colon, or skin cancers. They often appear as well-defined masses where gray and white brain matter meet, typically surrounded by swelling. Although surgeons can often remove these cleanly, their presence usually means the cancer has spread widely throughout the body, complicating treatment decisions [17]. As Figure 1.1 shows, glioblastoma, meningioma, and metastases look and behave quite differently, requiring different surgical approaches. But they share a common problem: during surgery, surgeons can't reliably see the exact boundaries between tumor and healthy tissue using current methods. This limitation highlights the urgent need for better tools that can distinguish tumor from healthy brain in real time, at the molecular level, without requiring special dyes or markers.

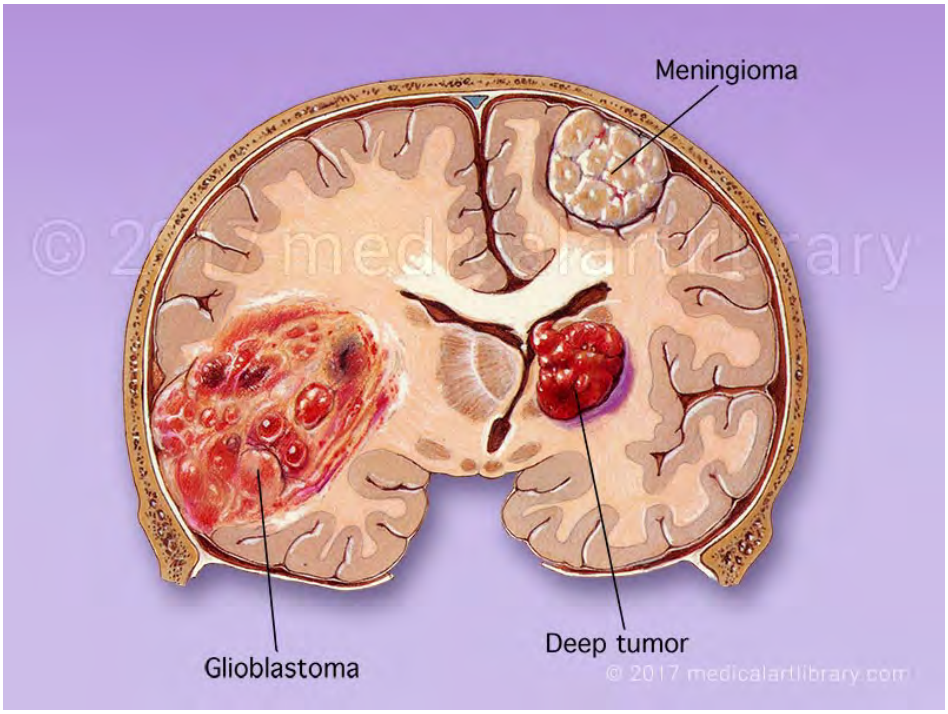

Figure 1.1 Illustration of common brain tumor types: glioblastoma multiform (infiltration, WHO Grade IV), meningioma (arising from the meninges), and brain metastasis (typically well-circumscribed lesions from systemic cancers). Adapted from the Medical Art Library.

Several technologies have emerged to help surgeons see tumors better during operations. These include intraoperative MRI (iMRI), fluorescence-guided surgery using 5-aminolevulinic acid (5-ALA), intraoperative ultrasound, and rapid tissue analysis. Each offers unique benefits but also has significant limitations that prevent truly precise, real-time molecular guidance during surgery. The following sections explore these techniques and their clinical applications.

1.1.1 Intraoperative MRI (iMRI)

Intraoperative Magnetic Resonance Imaging (iMRI) is an advanced imaging technique that enables real-time acquisition of high-resolution anatomical images during neurosurgical procedures. Its primary goal is to improve the extent of tumor resection by providing intraoperative feedback on residual tumor tissue, thereby reducing the need for re-operations and improving patient outcomes. iMRI operates using the same principles as conventional MRI; it exploits the magnetic properties of hydrogen nuclei in water molecules to generate detailed soft-tissue contrast. In the intraoperative setting, iMRI systems are typically implemented in one of three configurations: low-field (0.15–0.5 T), mid-field (0.5–1.0 T), or high-field (1.5–3.0 T) scanners. High-field systems offer superior spatial resolution but require greater shielding and infrastructure, often involving movable MRI gantries or specialized MRI-compatible operating rooms. Figure 1.2 illustrates a typical surgical workflow with the iMRI guidance. Preoperative scans are used to plan the surgical path, which is overlaid on the neuro navigation system and projected onto the surgical field. After the initial resection, an intraoperative scan was acquired to assess the residual tumor. If tumor remnants are identified, resection continues, guided by updated navigation based on the new images. Despite its utility, the iMRI presents several challenges. iMRI cannot reliably detect microscopic tumor infiltration, which is typical of GBM [28]. These systems are costly and require specialized infrastructure, including MRI-compatible surgical instruments, patient transfer systems, and ferromagnetic safety protocols [29]. Image acquisition and re-registration introduce workflow interruptions, often significantly extending the surgical duration [30]. In summary, while iMRI significantly enhances intraoperative visualization and surgical precision, its high cost, complexity, and limited sensitivity to biochemical alterations constrain its utility in routine clinical practice.

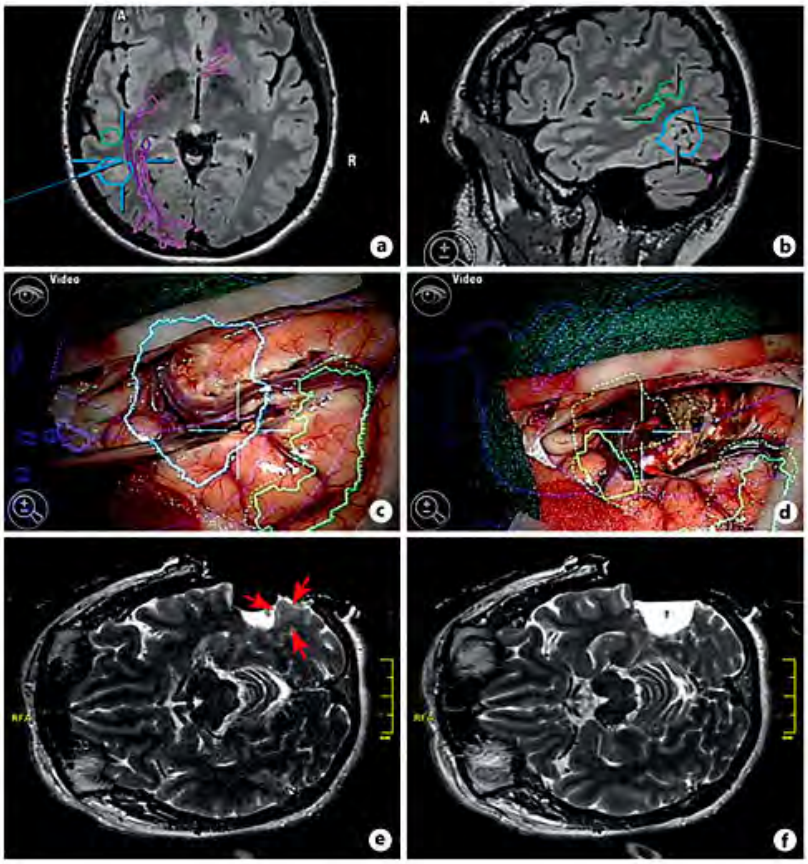

Figure 1.2 Figure shows how intraoperative MRI was used to guide the resection of a brain tumor located near critical functional areas. The images before surgery (a, b) highlight the tumor in light blue, along with nearby important regions, such as Wernicke's area (green) and visual pathways (purple and pink). The surgical plan, including the target point and path, was overlaid. During the operation, the neuro navigation system projected this information into the surgeon's microscope view (c), showing both functional areas and major blood vessels. The first round of imaging revealed that some tumor tissue remained (e, red arrows). After updating the navigation system with this new information, the surgery was continued. The adjusted microscope view (d) helped the surgeon focus on the remaining tumor area (outlined in yellow). Final images (f) confirmed that the tumor was completely removed [18].

1.1.2 5-Aminolevulinic Acid (5-ALA) Fluorescence Guidance

5-Aminolevulinic acid (5-ALA) is an FDA- and EMA-approved metabolic imaging agent widely used for the fluorescence-guided resection of malignant gliomas. 5-ALA is a naturally occurring intermediate in the heme biosynthetic pathway. When administered orally (usually 20 mg/kg) approximately 3–4 h before surgery, it selectively accumulates in tumor cells because of their altered mitochondrial metabolism. Within these cells, 5-ALA is enzymatically converted into proto-porphyrin IX (PpIX), a fluorescent compound that emits red

fluorescence (peak emission at approximately 635 nm) when excited by blue light (typically at approximately 405 nm). During surgery, the operating microscope is equipped with a blue light filter that excites PpIX, allowing the surgeon to visualize fluorescent tumor regions in real time. Figure 1.3 illustrates how fluorescence assists with distinguishing tumor margins under white light and blue light conditions. This fluorescence guidance enhances the surgeon's ability to identify malignant tissue uncooperatively, particularly in high-grade gliomas, and has been associated with significantly improved extent of resection (EOR) and progression-free survival in randomized clinical trials [31]. However, despite its clinical utility, 5-ALA fluorescence has several limitations. First, its efficiency varies according to tumor grade and cellularity. High-grade gliomas (WHO grade III–IV) typically accumulate sufficient levels of PpIX to be visualized, whereas low-grade gliomas and infiltrate tumor margins may exhibit little or no fluorescence due to reduced metabolic activity and lower mitochondrial content [30]. This can lead to an underestimation of the tumor extent in diffuse regions.

Second, fluorescence visualization is inherently qualitative and depends on the surgeon's interpretation of the images. The signal intensity is influenced by multiple factors, including tissue depth, angle of illumination, blood presence, cauterization artifacts, and optical scattering. Moreover, there is currently no quantitative threshold to define positive fluorescence, which can lead to inconsistent assessments of tumor margins [32]. Finally, because PpIX is photosensitive, patients must avoid bright-light exposure for up to 24 h postoperatively to reduce the risk of photo-toxicity. This requires special postoperative care and limits the patient throughput in some clinical settings. In summary, 5-ALA fluorescence guidance has proven effective in improving the resection of enhancing gliomas. However, its dependency on metabolic activity and visual inspection, as well as its inability to detect non-enhancing or infiltrate tumor regions, limit its application. These gaps highlight the need for label-free, biochemically sensitive imaging modalities such as Raman spectroscopy, which can detect molecular signatures independent of tumor metabolism.

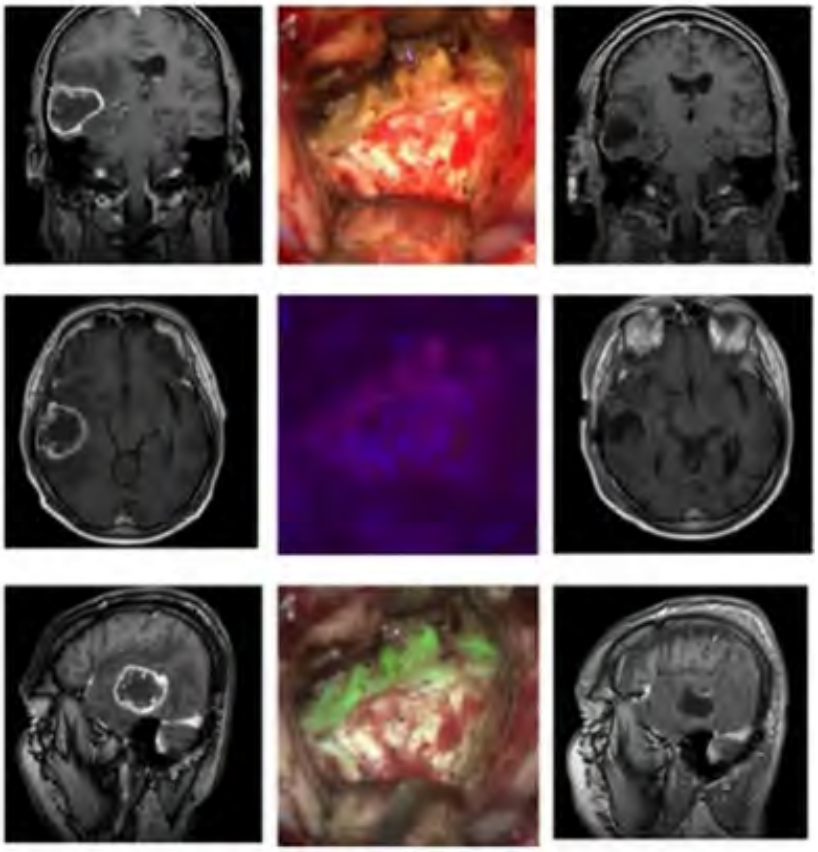

Figure 1.3 Preoperative MRI scans (left) display the tumor location, while postoperative images (right) confirm the extent of resection. The central column presents the surgical cavity. The top image shows the tumor under standard white light illumination, the middle image reveals the fluorescent signal under blue light, highlighting pinkish tones, and the bottom image displays a merged view using multi spectral fluorescence (MFL) mode, where the tumor appears in green pseudo-color. Reprinted from [19] with permission.

1.1.3 Intraoperative Ultrasound (IOUS)

Intraoperative ultrasound (IOUS) is a widely accessible and cost-effective imaging modality that provides real-time visualization of intracranial structures during neurosurgery. It operates by transmitting high-frequency acoustic waves (typically 5–15 MHz) into the brain tissue and recording the reflected echoes based on changes in the acoustic impedance at the tissue interfaces. These echoes are used to construct cross-sectional images that can assist in identifying the tumor location, shape, and boundaries.

IOUS is often used in conjunction with preoperative imaging data to guide craniotomy planning, navigate deep lesions, and verify tumor resection intraoperative. Its advantage lies in its ability to update the surgeon with real-time anatomical feedback. This can compensate

for brain shift that make preoperative MRI-based neuro-navigation unreliable as the surgery progresses.

As illustrated in Figure 1.4, IOUS can delineate tumor margins in high-grade gliomas, such as glioblastoma multi-forme (GBM), based on the echogenic contrast between the tumor and surrounding parenchyma. GBMs often appear hyperechoic due to their dense cellular structure and vascularity, making them distinguishable from normal brain tissue. However, this contrast can be reduced when tumors are necrotic, cystic, or mixed with surrounding edema, which complicates interpretation. Despite its real-time imaging capabilities, IOUS has several limitations. First, it is highly operator-dependent, requiring substantial experience to accurately interpret grayscale images in the context of evolving surgical anatomy [33]. Unlike MRI, ultrasound images are susceptible to artifacts, such as acoustic shadowing, signal dropout, and reverberation, particularly near bone or air-tissue interfaces. Second, IOUS has limited spatial resolution compared to MRI, particularly in detecting small residual tumor volumes at the margins [34]. Additionally, deeper lesions are more difficult to visualize because of signal attenuation with tissue depth. To address some of these issues, advanced IOUS techniques have been introduced, including contrast-enhanced ultrasound (CEUS), Doppler ultrasound for vascular mapping, and 3D ultrasound with image fusion to overlay intraoperative images onto preoperative magnetic resonance imaging (MRI). However, these enhancements remain limited to routine clinical neurosurgical use. In conclusion, IOUS remains a valuable adjunct in brain tumor surgery because of its portability, real-time feedback, and low cost. But, its dependence on image quality, user expertise, and lack of molecular specificity restricts its standalone utility in clinical practice. Integrating IOUS with complementary techniques, such as Raman imaging, may provide a more comprehensive intraoperative guidance framework.

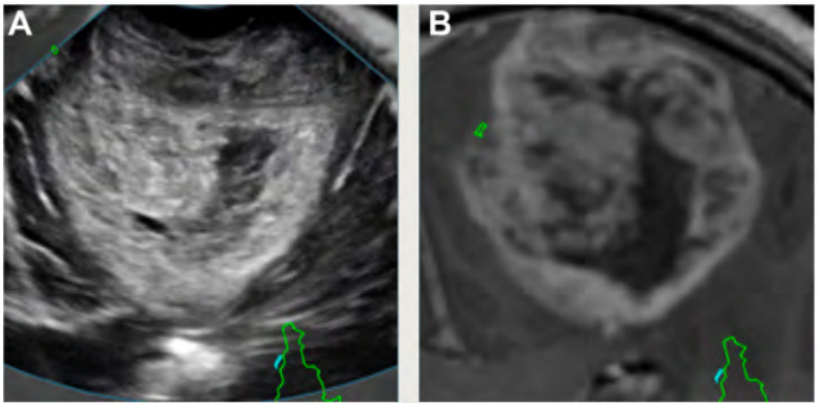

Figure 1.4 Example showing how a glioblastoma multiform appears in both intraoperative ultrasound and preoperative MRI. In this case, the tumor has a visibility grade of 3 in both the ultrasound image (A) and MRI scan (B), indicating clear and comparable visualization across both modalities. Image reprinted from [20] with permission.

1.1.4 Histopathology Analysis

Histopathology examination remains the clinical gold standard for the definitive diagnosis and classification of brain tumors. It enables the microscopic evaluation of cellular morphology, nuclear features, mitotic activity, tissue architecture, and patterns of infiltration, which are essential for determining the tumor type, grade, and aggressiveness. Figure 1.5 illustrates this process by comparing the intraoperative fluorescence findings with the matched histological sections. The most common staining technique is hematoxylin and eosin (H&E), which differentially stains nuclei (blue-purple) and the cytoplasm or extracellular matrix (pink), thereby providing a contrast for evaluating tissue organization. Additional immunochemistry stains are often used to identify specific molecular markers, such as IDH1 mutation, p53 overexpression, or GFAP positivity, further aiding classification according to the World Health Organization (WHO) central nervous system tumor classification guidelines. Histopatholoy analysis plays a key role in validating intraoperative findings and guiding postoperative treatment. However, this method has some limitations. First, it is inherently retrospective; tissue must be harvested, fixed in formalin, embedded in paraffin, sectioned, stained, and reviewed by a neuro-pathologist, a process that typically spans several hours to days. Consequently, it cannot provide real-time surgical guidance. Second, histology relies on small tissue samples that may not fully represent tumor heterogeneity. Sampling errors may occur, especially at the tumor margins, where malignant cells may be sparse or intermixed with normal tissue. Frozen section analysis, sometimes used intraoperative, offers more rapid feedback but with reduced image quality and potential diagnostic inaccuracy. Furthermore, histopathol-

ogy interpretation is subject to inter-observer variability, particularly for borderline or mixed tumor types. Although quantitative digital pathology and machine learning-based classifiers are being developed, their clinical deployment is still evolving.

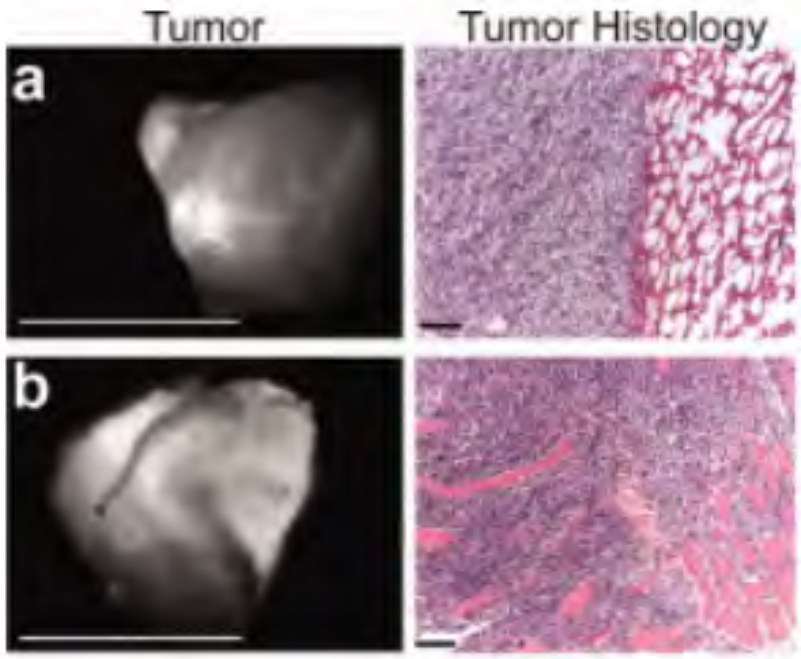

Figure 1.5 Comparison of tumor fluorescence and corresponding histology. (a) and (b) show two tumor samples imaged under fluorescence guidance (left) and their matched hematoxylin and eosin (H&E) stained histological sections (right). Fluorescence images highlight the tumor regions, while histology confirms the tissue structure and cellularity. Image reprinted from [21] with permission.

These limitations underscore the need for real-time, label-free, and molecularly specific imaging tools to guide neurosurgeons with high sensitivity and specificity. Raman spectroscopy, especially in its wide field and multispectral configurations, is uniquely positioned to address these unmet clinical needs [17, 25]. Based on recent developments in our laboratory [17, 25], this study aimed to repackage, validate, and clinically evaluate a new wide-field Raman imaging system customized for neurosurgical guidance.

The following sections outline the research hypothesis, underlying objectives, and structure of this thesis.

1.2 Research Hypotheses

Recent clinical studies have demonstrated that Raman spectroscopy can distinguish tumor tissue from non-tumoral brain tissue in situ with high diagnostic performance [17]. Although handheld point-based Raman probes have been successful in detecting molecular changes during surgery, their limited field of view and inability to provide spatial context restrict their effectiveness for comprehensive margin assessment. We hypothesize that a wide-field, multi spectral Raman imaging system is capable of acquiring spatially resolved Raman intensity maps at diagnostically significant spectral bands (e.g., 1004, 1299, 1340, and 1441cm^{-1}) that can deliver sufficient molecular contrast to differentiate tumors from normal brain tissue across a large surgical area [17]. The system incorporates a robust baseline correction technique developed in-house [25] that mitigates tissue auto fluorescence and enhances signal fidelity. Specifically, in this master project, we propose that the system will accurately detect Raman bands associated with lipids and proteins, particularly the CH_2/CH_3 deformation mode at approximately 1440 cm^{-1}—with high spatial uniformity and sensitivity. For brain tumor detection, this band alone yielded a sensitivity/specificity of 86%/77% with an AUC of 0.86, which is comparable to more complex multi band SVM models [17, 25]. Calibration and normalization using reference standards (e.g., NIST and Spectralon) will improve the quantitative accuracy across the field of view. When applied to ex vivo brain tissue samples, the spatial distribution of the Raman intensity is expected to correlate with histologically verified tumor margins.

1.3 Research Objectives

The primary objective of this project is to repackage and validate a wide-field Raman imaging system with a field of view (FOV) exceeding 2 cm^2, a spatial resolution of 350 μm, and capable of detecting the key Raman biomarker, CH_2/CH_3 lipid/protein bands at 1440cm^{-1}. This is based on the multi spectral Raman imaging developed by the LUMED laboratory [25].

1.3.1 Objective 1: Automate Signal Acquisition and Control

In the future, the system must be compatible with the surgical workflow, and therefore, it must support automated operation. Signal acquisition and processing must be fully controlled using custom Python software, which integrates all system components (laser, camera, and filter wheel) via serial and USB interfaces. In parallel to the future perspective of this project, this master's project aims to develop a GUI for filter wheel synchronization during acquisition.

1.3.2 Objective 2: To repackage and Integrate the System into a Standalone Clinical Unit

The existing multispectral Raman imaging system was redesigned to function as a compact, standalone platform independent of external laboratory infrastructure. This includes integrating a dedicated illumination module, mechanically stabilizing optical components, and ensuring modular portability for future in-hospital deployment.

1.3.3 Objective 3: To Assess System Performance Using Porcine/Muscle tissues

The standalone Raman imaging system was evaluated under controlled laboratory conditions using porcine muscle and fat tissues as representative analogs of human brain tissue composition. Performance assessment will focus on key metrics, including detection accuracy, measurement repeatability, and signal fidelity, particularly at the 1440 cm^{-1} Raman band, which is associated with lipid and protein content. A dedicated data processing pipeline will be developed and validated at each stage, from raw data acquisition to final image reconstruction and interpretation. This pipeline includes steps such as background subtraction, spatial and spectral correction, normalization, and intensity mapping. The objective was to identify the most optimized filter configuration and acquisition strategy tailored to the optical and biochemical properties of muscle and adipose tissues, thereby establishing a robust framework for future ex vivo studies.

1.3.4 Objective 4: Clinical Evaluation During Pilot Study

To demonstrate clinical feasibility, the system will be used in a pilot study at the Montreal Neurological Institute (MNI) to perform ex vivo measurements on different brain tumors. To achieve this, a robust image registration protocol and a detailed image registration workflow must be developed to spatially align wide-field multi spectral samples with their corresponding histopathological sections. This process includes the use of fiducial markers, scale normalization, and manual or semi-automated alignment techniques to ensure correspondence between the Raman data and annotated histology images. Accurate registration is critical for validating the spatial specificity of Raman spectroscopy relative to confirmed tumor margins.

Objective 4.1: Conduct Preliminary Diagnostic Evaluation

A qualitative evaluation was conducted, and a data processing pipeline was implemented to assess the system's ability to distinguish tumor from non-tumor tissue by comparing Raman intensity maps at 1440 cm^{-1} with histopathology annotated ground truth. This

objective aims to demonstrate the feasibility and spatial reliability of the Raman signal in capturing relevant biochemical contrasts within brain tissue. Owing to the limited sample size, quantitative performance metrics, such as sensitivity and specificity, are not reported at this stage but are intended for future studies.

1.4 Thesis Organization

The first chapter presents the clinical motivation, existing intraoperative guidance technologies, and limitations of the current approaches in brain cancer surgery. In the second chapter, we cover light-tissue interaction, principles of Raman spectroscopy, and wide-field Raman imaging technologies. In the third chapter/system design and development, we detail the implementation of Objectives 1 and 2, covering hardware integration, optical design, and automation software for a standalone multi spectral Raman imaging system. Chapter four/Preclinical Validation) addresses Objective 3 by evaluating the system's performance on porcine tissue samples, including calibration, signal correction, and Raman image analysis. Chapter five/Clinical Application and Pilot Testing: Focuses on Objective 4, presenting ex vivo data acquired at MNI, image registration procedures, and qualitative comparison of Raman and histopathology data. Chapter six/ Discussion and Conclusion: Summarizes the findings, discusses technical and clinical implications, and outlines future directions for large-scale validation and clinical deployment.

CHAPTER 2 LITERATURE REVIEW

2.1 Light–Matter Interactions

When imaging biological tissues, it is important to have a deep understanding of how light interacts with tissues. Light-tissue interactions can be categorized into different optical phenomena: Fluorescence, Absorption, Reflection, Refraction, and Scattering. The analysis of these light interactions with the tissue provides insight into the metabolic and pathological states of the tissue [35].

2.1.1 Fluorescence

Luminescence is the emission of light from any substance that occurs in electronically excited states. Luminescence depends on the nature of the excited state and is divided into two categories: phosphorescence and fluorescence.

Phosphorescence is the emission of light from triplet excited states, in which the electron in the excited orbital has the same spin orientation as the ground-state electron. Transitions to the ground state are forbidden, and the emission rates are slow (10^3 to 100 s^{-1}), so phosphorescence lifetimes are typically in the millisecond to second range.

Fluorescence is the emission of light from singlet states, the electron in the excited orbital is paired (by opposite spin) to the second electron in the ground-state orbital. Consequently, the return to the ground state is spin-allowed and occurs rapidly by the emission of a photon. The emission rates of fluorescence are typically 10^{-8} s^{-1}; therefore, a typical fluorescence lifetime is approximately 10 ns (10×10^{-9} s). Fluorescence typically occurs in aromatic compounds. Common fluorophores include quinine (found in tonic water), fluorescein (used in environmental monitoring and emergency markers), and various dyes used for DNA staining and laser applications. Fluorophores are divided into two general classes: intrinsic and extrinsic. Intrinsic fluorophores occur naturally. Extrinsic fluorophores are added to a sample that does not display the desired spectral properties [36]. Intrinsic or extrinsic fluorophores have a higher emission wavelength than absorption. Fluorescence spectroscopy provides metabolic information about biological tissues, making it an applicable diagnostic technique.

2.1.2 Absorption

Light absorption is the transfer of electromagnetic energy from light to the matter. Absorption occurs when the energy of the incident photons matches the energy difference between

the two quantum states of the material:

$$E = h\nu = \frac{hc}{\lambda} \tag{2.1}$$

where h is Planck's constant, ν is the frequency of light, λ is the wavelength of light, and c is the speed of light [37].

Absorption is defined in different ways. **Electronic Absorption** occurs when photons excite electrons from a lower energy state to a higher energy state, typically observed in the UV-Vis region [38]. In **vibrational absorption**, photons excite molecular vibrations and are typically observed in the infrared (IR) region [37]. Another type of absorption occurs in the microwave region, corresponding to changes in the rotational energy levels of molecules [37], which is known as **rotational absorption**.

Principles of Absorption

Absorption Coefficient Macroscopically, absorptive materials are described by the absorption coefficient μ_a, defined as the probability of photons being absorbed when traveling over a certain distance within the tissue. For homogeneous materials, a collection of absorbing particles can be considered as a collection of absorbers, each having an absorption cross-section, a_a, given by:

$$a_a = \frac{P_{\text{abs}}}{I_0}, \tag{2.2}$$

where P_{abs} is the absorbed power in [W], and I_0 is the intensity of the beam of light that enters, in [W / mW / mW / m^2]. Using the above equation, we can express μ_a for a tissue composed of a large number of identical absorbing particles as follows:

$$\mu_a = \frac{N \cdot a_a}{V}, \tag{2.3}$$

where μ_a depends on the wavelength of light used and is characteristic of each tissue type. The reciprocal of μ_a is called the absorption mean free path, l_a:

$$l_a = \frac{1}{\mu_a}, \tag{2.4}$$

describes the average distance traveled by a photon before it is absorbed.

The Beer-Lambert Law The Beer-Lambert law defines the absorbance, A, of a medium as

$$A = \epsilon \cdot c \cdot h, \tag{2.5}$$

where ϵ is the molar absorptivity in [L/(mol $\cdot$ m)], c is the molar concentration in [mol/L], and h is the thickness of the medium in [m]. Absorbance, which defines the capacity of a medium to absorb light, is a concept typically used in chemistry. In physics, a similar concept is expressed in terms of the optical depth:

$$\tau = \mu_a \cdot h. \tag{2.6}$$

τ represents the attenuation of light traveling a distance h within the medium. For an infinitesimally small slab of material with thickness dh, the attenuation due to absorption is proportional to the optical depth, resulting in a loss of light intensity.

$$dI = -\alpha_{\text{ap}} I dh = -\mu_a I dh, \tag{2.7}$$

which, upon integration, yields

$$I(h) = I_0 e^{-\alpha_{\text{ap}} h} = I_0 e^{-\mu_a h}, \tag{2.8}$$

where $I_0 = I(h = 0)$ is the intensity of light incident on the material.

Factors Influencing Absorption Absorption is wavelength-dependent, meaning that it occurs only when the photon energy matches the energy gap of the tissue. [34]. Material composition also affects absorption; chromophores such as hemoglobin and melanin determine tissue absorption spectra [39]. Temperatures also broaden the absorption lines due to Doppler and collisional effects [38]. Absorption increases with the concentration of the absorbing species according to the Beer-Lambert Law [37].

Light Penetration and Absorption in Biological Tissue

In biological tissues, light penetration is governed by both absorption and light scattering. The depth to which photons can propagate before being absorbed or scattered out of the collection path depends strongly on the absorption coefficient μ_a and the reduced scattering coefficient μ_s'. These coefficients are tissue-specific and dependent on the wavelength. For

brain tissue at 785 nm, the typical values are $\mu_a = 0.01$ mm^{-1} and $\mu_s' = 1$ mm^{-1}, indicating relatively low absorption but moderate scattering in the near-infrared region [34, 40]. Under these conditions, simulation and experimental studies using Monte Carlo models have shown that most detectable photons originate from depths shallower than approximately 600µm. This is due to the cumulative effect of absorption and multiple scattering, which limits the effective sensing volume to sub-millimeter depths [40].

2.1.3 Reflection and Refraction

When light interacts with biological tissues, its propagation is influenced by the optical properties of the medium, such as the refractive index, surface roughness, and tissue composition. Two fundamental optical phenomena, *reflection* and *refraction*, play key roles in understanding how light propagates through and interacts with tissues. These processes are integral to various biomedical applications, including imaging, diagnostics, and therapeutic techniques [33].

Specular Reflection Specular reflection occurs when light strikes a smooth surface with irregularities smaller than the wavelength of the incident light. This reflection follows Snell's law, where the angle of reflection (θ_r) equals the angle of incidence (θ_i):

$$\theta_r = \theta_i. \tag{2.9}$$

Fresnel Equations The Fresnel equations describe the fraction of light reflected at the interface between two media with refractive indices n_1 and n_2 as follows: The reflection coefficients for light polarized parallel ($R_\parallel$) and perpendicular ($R_\perp$) to the plane of incidence are given by

$$R_\parallel = \left(\frac{n_2 \cos\theta_i - n_1 \cos\theta_t}{n_2 \cos\theta_i + n_1 \cos\theta_t} \right)^2, \tag{2.10}$$

$$R_\perp = \left(\frac{n_1 \cos\theta_i - n_2 \cos\theta_t}{n_1 \cos\theta_i + n_2 \cos\theta_t} \right)^2, \tag{2.11}$$

where θ_t is the transmission angle. Specular reflection is dominant on smooth tissue surfaces, such as the cornea or internal organs with a fluid interface.

Diffuse Reflection Diffuse reflection occurs when light interacts with rough surfaces where the surface irregularities are on the order of or larger than the wavelength of light. In biological tissues, this is a common phenomenon owing to the heterogeneous structure of the

tissue, including cellular and subcellular components [33]. Diffuse reflection arises from multiple scattering events caused by cell membranes and organelles, collagen fibers, nuclei, and cytoplasm interfaces. Diffuse reflection is critical in diagnostic techniques, such as diffuse reflectance spectroscopy (DRS), which provides information about tissue composition and structure.
In wide-field Raman imaging systems, such as those developed for label-free tissue characterization, diffuse reflection plays a dual role. First, it acts as a **background signal** that can interfere with the detection of weak Raman photons, particularly in the presence of high-scattering structures, such as white matter or collagen-rich regions. Second, and more importantly, diffuse reflectance carries valuable **optical and structural information** about the tissue that can be used to normalize and calibrate Raman signals.

2.1.4 Scattering

Scattering is the interaction between light and matter at frequencies outside resonance. Suppose that the energy of the incident photon does not match the energy level difference required for absorption. In this case, the incident electromagnetic wave can still excite the electronic cloud of the molecule into an oscillating dipole. This oscillating dipole emits radiation, a phenomenon known as scattering. The interaction of an incident photon with a molecule is represented in the Jablonski diagram by the creation of a virtual state, V. Virtual states (V) are extremely short-lived, unobservable quantum states that are used as intermediate states in multi-step processes, such as scattering or nonlinear interactions. Their lifespan is extremely short and can be estimated to be approximately 1×10^{-16} s using uncertainty relations. In the Jablonski diagram, virtual states are represented by dashed lines.
Scattering does not result in atomic or molecular transitions. Instead, it consists of the oscillation of the electron cloud at the frequency of the incident photon, which can be modulated by the nuclear motion. These oscillations are followed by the re-emission of the original (or modulated) light quantum. Scattering also changes the direction of propagation of incident electromagnetic waves. After several scattering events, the path of the light is significantly altered, resulting in collimated and coherent beams becoming diffuse and incoherent.
Scattering can be classified into two main types:elastic and inelastic.

- **Elastic Scattering**: No energy transfer occurs between the wave and the medium. The scattered photons have the same energy (or wavelength) as the incident photons.
- **Inelastic Scattering**: Energy transfer occurs between the wave and the medium. The scattered photon has a different energy (or wavelength) than the incident photon.

Rayleigh scattering is an approximation that explains the scattering of light by particles that are much smaller than the wavelength of the incident light. These particles can include atoms or molecules in solids, liquids, or gases, such as nitrogen and oxygen molecules. The oscillations of the particle charges induced by the electric field of light lead to re-emission at the same frequency.

The scattering cross-section for Rayleigh scattering is proportional to the inverse fourth power of the wavelength:

$$\sigma_s \propto \frac{1}{\lambda^4}. \tag{2.12}$$

This relationship explains why shorter wavelengths (e.g., blue light) are scattered more effectively than longer wavelengths (e.g., red light), resulting in phenomena such as the blue color of the sky.

Raman Scattering Raman scattering is an inelastic scattering process discovered by Sir C.V. Raman. When a photon interacts with a molecule, the energy of the scattered photon can be lower (Stokes shift) or higher (anti-Stokes shift) than that of the incident photon, corresponding to energy transfer to or from the vibrational modes of the molecule. Raman scattering provides a molecular fingerprint based on vibrational energy levels, enabling material identification and characterization.

Figure 2.1 illustrates the energy transitions involved in infrared absorption, Rayleigh scattering, and Raman scattering (Stokes and anti-Stokes shifts). Below is a detailed explanation:

In **Infrared Absorption**, a photon with energy $h\nu_{\text{vib}}$ excites the molecule from its ground vibrational level (S_0) to a higher vibrational level within the same electronic state. This is a resonant process that involves real transitions between vibrational energy levels.

Rayleigh Scattering occurs when an incident photon with energy $h\nu_0$ interacts with the molecule, exciting it to a virtual energy state. The molecule then immediately re-emits a photon of the same energy ($h\nu_0$). Because the scattered photon has the same energy as the incident photon, Rayleigh scattering is an **elastic scattering** process, meaning that there is no energy transfer between the photon and the molecule. The molecule remains in its original energy state after the scattering.

Raman Scattering is an **inelastic scattering** process where the energy of the scattered photon differs from that of the incident photon. Two cases are observed:

- **Stokes Raman Scattering**: An incident photon ($h\nu_0$) excites the molecule to a virtual energy state, and the molecule transitions to a higher vibrational energy level ($h\nu_{\text{vib}}$) after scattering. The scattered photon has lower energy than the incident photon,

resulting in a **red-shifted** photon with energy $h(\nu_0 - \nu_{\text{vib}})$.

- **Anti-Stokes Raman Scattering**: If the molecule is initially in an excited vibrational energy state ($h\nu_{\text{vib}}$) before interacting with the photon, the scattered photon will gain energy as the molecule transitions to a lower vibrational energy state. The scattered photon has a higher energy than the incident photon, resulting in a **blue-shifted** photon with energy $h(\nu_0 + \nu_{\text{vib}})$.

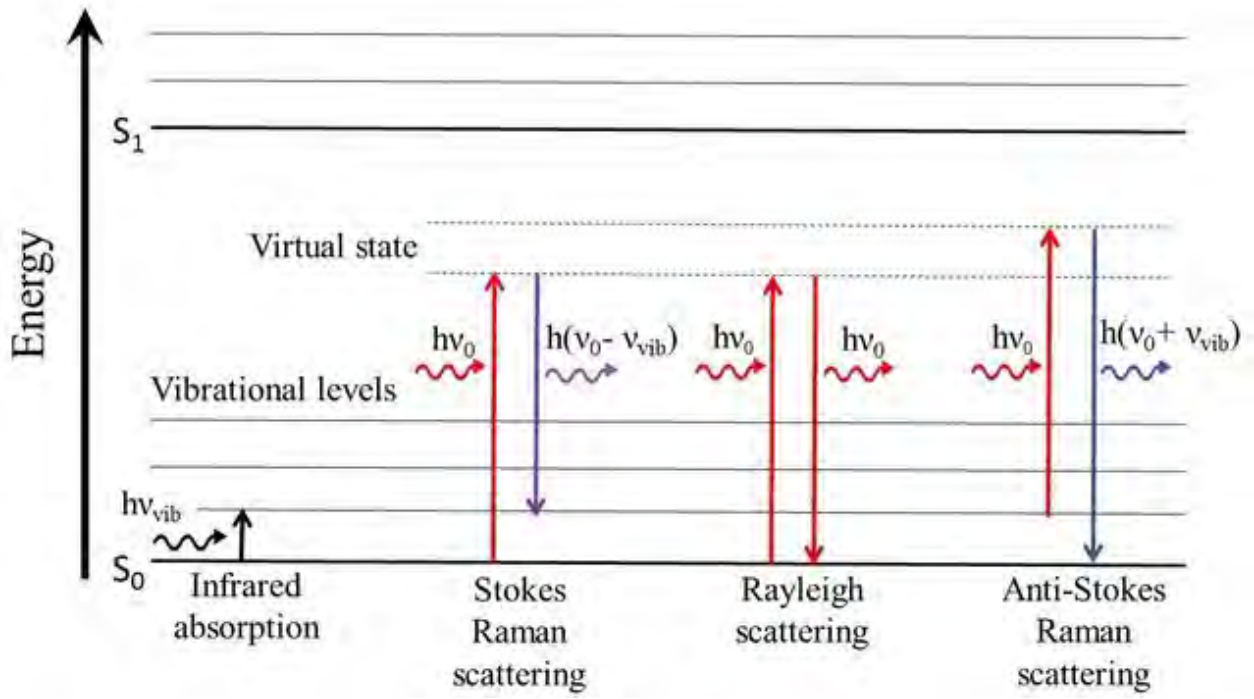

Figure 2.1 Jabolonski diagrams for Rayleigh and Raman scattering and Infrared absorption [22].

2.2 Raman Spectroscopy and Imaging Systems

Macroscopic Raman imaging, covering areas larger than 1 mm^2, has gained popularity due to advancements in the sensitivity of the cameras and the accessibility of lasers. Macroscopic imaging enables the examination of large fields of view (FOVs) up to 1 cm^2, providing efficient molecule-specific information. A typical setup for such a system includes a laser as the excitation source to generate Raman scattering in the sample, a sensor (such as a camera or photodiode) to detect the scattered light, and a dichroic beam splitter to merge the excitation and collection optical paths at the sample position. Other essential components include a low-pass filter to eliminate residual Rayleigh scattering, a tunable filter to isolate and measure the

Raman spectral features, and various collection and excitation optics. Additional equipment may be required, depending on the selected imaging configuration.

2.2.1 Imaging Configurations

Three primary configurations are commonly used for Raman imaging, as illustrated in Figure 2.2.

1. **Raster Scanning (Fig. 2.2A):** This involves collecting a spectrum at each point within the FOV by scanning in a two-dimensional grid. Each measured point corresponds to a pixel in the hyperspectral image.

2. **Line Scanning (Fig. 2.2B):** In this method, a single line of the sample is analyzed at a time. The line is projected onto a two-dimensional sensor, with one axis representing the spectral features and the other representing the spatial positions along the line. Scanning the line across the sample allows complete FOV coverage.

3. **Wide-Field Imaging (Fig. 2.2C):** Here, the entire FOV is illuminated, and intensity images are captured directly. Hyperspectral images are constructed by acquiring intensity data at different wavelengths using a tunable filter or filter wheel placed in front of the sensor.

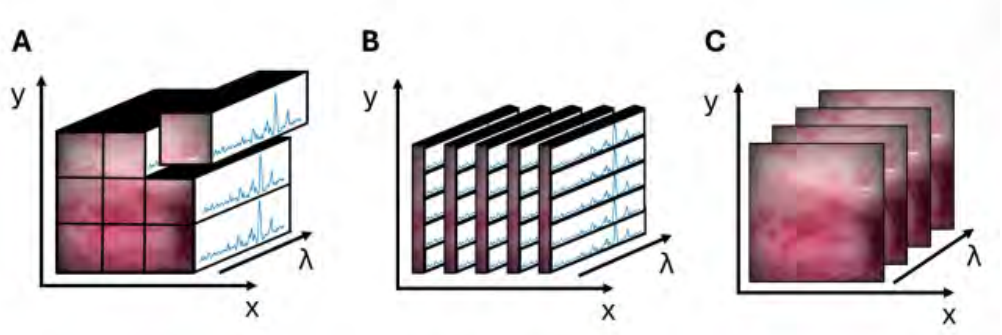

Figure 2.2 Three primary configurations for Raman macroscopically Imaging [23].

2.3 Raman in Neurosurgical Applications

Raman spectroscopy has emerged as a powerful tool in neurosurgery, offering real-time, label-free molecular insights to improve the precision of brain tumor resections. This technology is primarily implemented using two modalities: handheld Raman probes and Raman macroscopic imaging systems.

2.3.1 Raman Probes

Handheld Raman probes are fiber-optic devices designed for intraoperative use, enabling surgeons to differentiate between tumor and normal brain tissues in real-time [17,41]. As shown in Figure 2.3, handheld Raman spectroscopy was used to analyze brain tissues during surgery. These probes consist of optical fibers that deliver laser light to the tissue and collect scattered Raman signals. The collected signals are analyzed to identify the molecular compositions [41]. By analyzing the unique Raman spectra of different tissues, the probes can detect variations in biochemical composition, such as proteins, lipids, and nucleic acids, which are indicative of the presence of tumors [17]. The probes assist in delineating tumor boundaries, ensuring maximal resection of cancerous tissue while preserving healthy brain tissue. This is crucial for preventing tumor recurrence and maintaining neurological function [41]. They provide immediate feedback during surgery, reducing the reliance on time-consuming histopathology analyses [17].

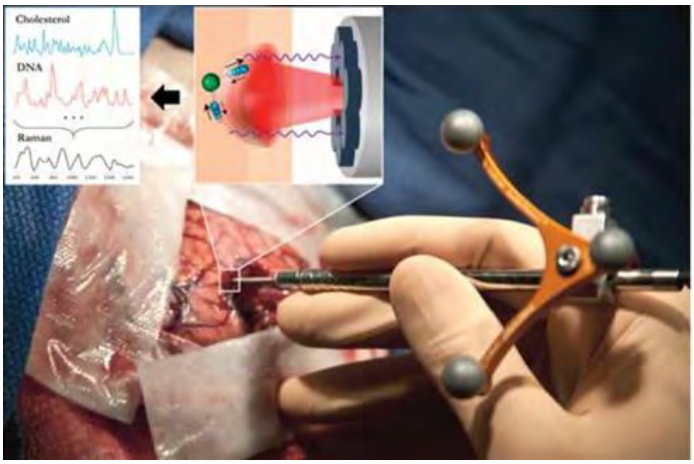

Figure 2.3 The handheld fiber-optic probe for Raman spectroscopy, developed by Emvision, LLC, was utilized to analyze brain tissue during surgical procedures. A schematic diagram on top-left depicting how the probe excites various molecular components, including cholesterol and DNA, to generate Raman spectra distinguishing cancerous tissue from normal brain tissue, as described by Jermyn et al. [24].

Case Study: The Sentry System The Sentry system is a recent clinical research study conducted by Leblond's group, in which a handheld Raman probe demonstrated significant potential in a multi center study involving 67 patients with glioblastoma, brain metastases, or meningioma. The device includes a conical probe tip for direct tissue contact, near-infrared (NIR) laser excitation at 785 nm, integration with a spectrometer, and machine learning algorithms. The system achieved diagnostic accuracies of 91% for glioblastoma, 97% for brain metastases, and 96% for meningioma. The real-time feedback provided by the Sentry System improves tumor detection and reduces the reliance on traditional histopathology methods [17]. The experimental workflow is shown in Figure 2.4.

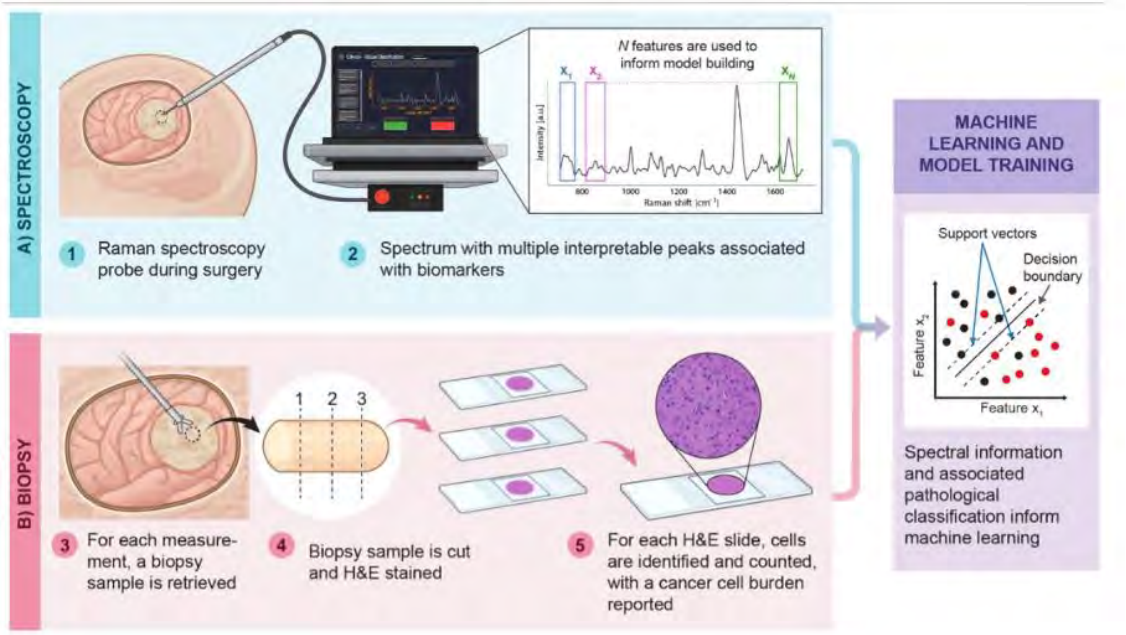

Figure 2.4 The experimental workflow for brain tumor detection with the Sentry System includes distinct processes. The blue section highlights the acquisition of spectral fingerprints using a handheld probe during neurosurgical procedures. The red section details the histopathology workflow, where each spectral measurement is matched with the corresponding data, including a pathologist's assessment of the cancer cell burden. Bulk tumor tissue is classified as having more than 90% cancer cell burden, while non-tumor brain tissue is defined by a 0% cancer cell burden. The green section illustrates the Sentry System's application in the real-time classification of tumor versus non-tumor brain tissue [17].

2.3.2 Wide-Field Raman Imaging Systems

Wide-field Raman imaging systems are designed to address the limitations of single-point Raman spectroscopy by providing spatially resolved molecular information across large fields of

view (FOV) [42]. These systems are highly effective for intraoperative use, enabling surgeons to rapidly differentiate between cancerous and non-cancerous tissues in real time, thereby significantly enhancing surgical outcomes.

The effectiveness of wide-field Raman imaging has been demonstrated in two studies conducted by Dr. Leblond's team, featuring the Macroscopic Line-Scanning Raman Imaging System and the Multi-Spectral Raman Imaging System, which are explained in the following sections.

Macroscopic Line-Scanning Raman Imaging System

Daoust et al. presented a macroscopic line-scanning Raman imaging system tailored for intraoperative tissue characterization [14]. This system emphasizes practicality and compliance with surgical workflows, focusing on safety and efficiency (Fig. 2.5. The system covers a 1 cm^2 area with a spatial resolution of 250 μm and a spectral resolution of 8 cm^{-1}, ensuring detailed molecular mapping of tissue regions. It includes a sterilizable probe mounted on an articulated arm for precise positioning and ease of use during surgery. This system can acquire Raman fingerprint images comprising 40 $\times$ 42 pixels in less than 5 min, ensuring minimal disruption to the surgical workflow. It also employs supervised machine learning models, such as Support Vector Machines (SVM) and Random Forests (RF), to classify tissue types with high accuracy. A tumor detection model trained on 352 in vivo single-point spectra (24 patients) was used to generate Cancer Likelihood Maps by computing the tumor probability for each Raman spectrum. Three key spectral features include **1004 cm^{-1}**: Phenylalanine ring breathing (protein marker), **1340 cm^{-1}**: Tryptophan/collagen-associated CH deformations, and **1430–1460 cm^{-1}**: CH_2/CH_3 deformation, sensitive to lipid/protein ratio, were used to train the classifier.

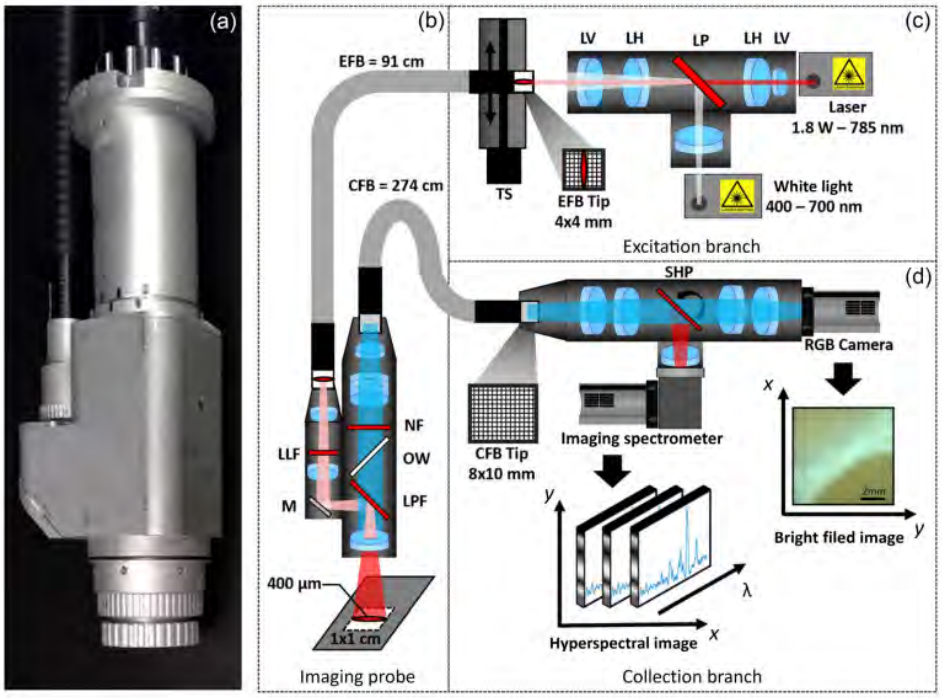

Figure 2.5 Overview of the handheld Raman imaging probe and system schematic. (a) Ergonomic handheld probe integrating illumination and collection optics. (b) The internal configuration includes an excitation fiber bundle (EFB), laser line filter (LLF), mirror (M), and long-pass filter (LPF) for delivering both laser and white light to the tissue for fluorescence excitation. On the collection side, a second LPF, optical window, and notch filter isolate the returning Raman signal, which is transmitted via a collection fiber bundle (CFB). (c) The excitation branch formed a line-shaped laser pattern and injected white light into the EFB mounted on a translation stage (TS). (d) The collection branch separates the white light and Raman signals using a scanning high-pass filter; the white light is directed to an RGB camera for structural imaging, whereas the Raman spectra are acquired using an imaging spectrometer. Spherical lenses are unlabeled, whereas cylindrical lenses are marked with LH (horizontal curvature) or LV (vertical curvature). Adapted from [14, 15]

Multi-Spectral Raman Imaging System

David et al. developed a non-contact, wide-field Raman imaging system that integrates multi-spectral imaging with advanced fluorescence background subtraction techniques [25]. The system is specifically designed to provide fast, high-resolution imaging over large tissue areas, making it suitable for real-time cancer detection. The key features of this system are as follows: first, a FOV of approximately 2 cm^2 with a spatial resolution of 350 μm, making it ideal for scanning broad areas of tissue during surgery. Second, the capability of imaging individual Raman spectral bands in less than a minute significantly reduces the

time required for intraoperative imaging. Thirdly, the system can isolate cancer biomarkers by targeting key Raman bands, such as lipid/protein bands (1302, 1440, and 1657 cm^{-1}), and phenylalanine (1004 cm^{-1}), which are strongly associated with tumor biochemistry. The system was validated using porcine tissue samples to differentiate between adipose and muscle tissues. Its ability to precisely identify biochemical differences demonstrates its potential for use in surgical settings, including brain, breast, lung, and gynecological cancer surgery.

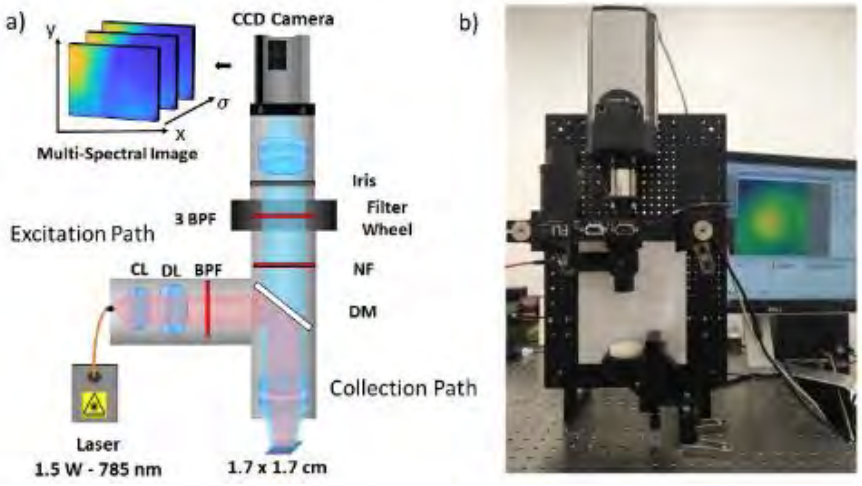

Figure 2.6 Experimental setup enabling multi-spectral detection of inelastic scattering in biological tissues: (a) A schematic diagram illustrating an epi-illumination configuration. The excitation path included an optical fiber, collimating lens (CL), band-pass filter (BPF), diverging lens, dichroic mirror (DM), and focusing lens. The collection path comprises a notch filter (NF), a filter wheel with nine interference band-pass filters, and a CCD camera. (b) A photograph of the system [25].

2.4 Limitations in Current Technologies

Despite the promising results of both the handheld Sentry system and the Macroscopic Line-Scanning Raman Imaging system, each platform presents practical limitations that motivated the development of the modified multi spectral imaging system described in this thesis. Although the Sentry probe offers real-time, point-based classification with high diagnostic accuracy, it is inherently limited by its small sampling volume and lack of spatial context. This restricts its ability to guide the resection margins over larger tissue areas. In contrast, the line-scanning system enables wide-field imaging but requires several minutes to acquire a single spectral map, which may introduce delays during time-sensitive surgical procedures and reduce intraoperative feasibility. In contrast, the updated multi spectral system presented

here aims to bridge these gaps by combining the advantages of non-contact, large field-of-view imaging with fast acquisition times at selected Raman bands. This design enables rapid molecular mapping across broad tissue regions while maintaining clinical workflow compatibility, thereby laying the groundwork for future real-time applications in brain tumor surgery.

CHAPTER 3 SYSTEM DESIGN AND DEVELOPMENT

The original Multi-Spectral Raman Imaging System developed by David et al. showed strong potential for wide-field, label-free tissue characterization but it relied on the lab's Biofluide imaging platform, for its illumination pathway. This limits its use to a controlled laboratory setting. As part of this thesis, I re-engineered the system as a stand-alone unit. My contributions included decoupling the system from the Biofluide platform by integrating a dedicated optical-fiber-based illumination subsystem, optimizing optical alignment, and enhancing mechanical stability for transport and deployment. In addition, I also implemented a robust calibration protocols, both spectral and spatial, to ensure reproducible performance across acquisition sessions. These modifications were critical for transitioning the system from proof-of-concept to clinical readiness, enabling its future evaluation in neurosurgical operating rooms and other hospital environments.

The following sections describe the key components of the multi spectral Raman imaging system: the laser source, camera, filter wheel, and full optical layout for the illumination, collection, and detection paths. Each component is presented in the context of its role in achieving fast, stable, and wide-field Raman imaging that is suitable for future clinical integration.

3.1 Optical Design and Components

3.1.1 Laser Illumination Source

A high-performance laser module from Innovative Photonic Solutions (IPS) provides a spectrum-stabilized output at 785 nm in the Raman imaging system. This Class 4 laser delivers up to 2500 mW and a spectral linewidth of less than 0.2 nm, suitable for precise excitation in multi spectral Raman imaging. Optical and safety specifications, as described in the manufacturer specifications [43] are as follows:

- Center Wavelength: 785 nm (typical), tolerance ± 0.5 nm
- Spectral Linewidth: < 0.2 nm
- Output Power: Up to 2500 mW
- Beam Divergence: 10–20 degrees
- Maximum Permissible Exposure (MPE): 1.9 mW/cm^2

- Nominal Ocular Hazard Distance (NOHD): 140 cm

The system is enclosed for user safety, and laser-protective eye-wear is required during operation. The stability and power of the laser ensured consistent excitation, which is especially important for detecting weak Raman signals with high spatial and spectral precision.

3.1.2 CCD Camera: Andor iKon-M 934

The **Andor iKon-M 934** CCD camera was selected for its high sensitivity and low noise essential for detecting weak raman signals. It features a 1024 × 1024 pixel back-illuminated sensor with 13 μm square pixels, resulting in a total active imaging area of 13.3 mm × 13.3 mm. This configuration offers a well-balanced compromise between the spatial resolution and photon-collection efficiency.

The camera is thermo-electrically cooled to **-60 °C** reducing the dark current as low as 0.00012 e^-/pixel/s. It supports multiple-pixel readout rates (0.05-5 MHz), with a typical read noise as low as **2.9 e^-** at the lowest readout speed, allowing high dynamic range detection. The digitization depth of 16-bit supports high-precision signal quantification.

The iKon-M 934 camera integrated an internal mechanical shutter and was connected via USB 2.0. It is equipped with a standard C-mount for lens or fiber coupling, which makes it adaptable to various optical setups. This camera also supports **Fringe Suppression Technology™**, reducing interference effects in near-infrared Raman imaging, which is beneficial when imaging at 1004 cm^{-1} and 1440 cm^{-1} bands.

In this setup, the BEX2-DD (deep depletion) sensor version was used to maximize the quantum efficiency in the near-infrared region. In addition, the extended-range anti-reflective (AR) coatings cover the full visible to NIR spectrum. The low dark current and broad spectral response make this camera particularly well-suited for long-exposure multi spectral Raman imaging of biological tissues.

Table 3.1 Key Specifications of the Andor iKon-M 934 Camera

Parameter	**Value**
Sensor Type	Back-illuminated CCD (BEX2-DD)
Pixel Array	1024 × 1024
Pixel Size	13 μm × 13 μm
Active Area	13.3 mm × 13.3 mm
Cooling	Down to -100°C (TEC)
Read Noise	2.9–18 e^- (depending on readout rate)
Digitization	16-bit
Interface	USB 2.0
Mount	C-mount
Shutter	Internal mechanical shutter
Fringe Suppression	Yes (BEX2-DD models)

3.1.3 Filter Wheel: FLI High Speed Filter Wheel

A **high-speed filter wheel (HSFW)** manufactured by Finger Lakes Instrumentation (FLI) is another key component of the Raman imaging system. The HSFW uses a high-torque servo motor and a DSP-based controller to achieve fast and accurate filter transitions with minimal vibration. Filter switching times as low as 23–30 milliseconds between adjacent positions allow real-time imaging across multiple Raman bands.

Each filter wheel can hold circular optical filters of 25 -32 mm diameter and supported thicknesses of 1–9 mm, depending on the model. The filter wheel used in this project incorporated the HS-1025 model with 25 mm filters. The filter positions are controlled through an RS-232 serial interface with daisy-chain support for up to three wheels operating on a single port. Simple byte commands control the positioning and can be automated through custom software via PyVISA and Python GUI integration.

The HSFW maintains consistent performance under varying mechanical loads (filter size and weight) owing to its built-in adaptive control algorithm. This ensures high reliability, even during continuous operation in a surgical imaging environment.

For this system, the HSFW is synchronized with the camera and laser via software control to enable precise mult ispectral acquisition. The device is powered by a dedicated 24V DC adapter and configured with standard RS-232 communication settings (9600 baud, 8 data bits, 1 stop bit, no parity) [44].

3.2 Hardware-Software Synchronization

3.2.1 Automation and Control of Filter Wheel via Python

To control band-pass filter selection, I developed a custom graphical user interface (GUI) using Python 3.1. This module allows the user to connect to the filter wheel via a serial (USB) port, select one or more filter positions, and send the control commands directly to the hardware. The implementation uses the `PyVISA` library for communication and `PyQt5` for GUI.

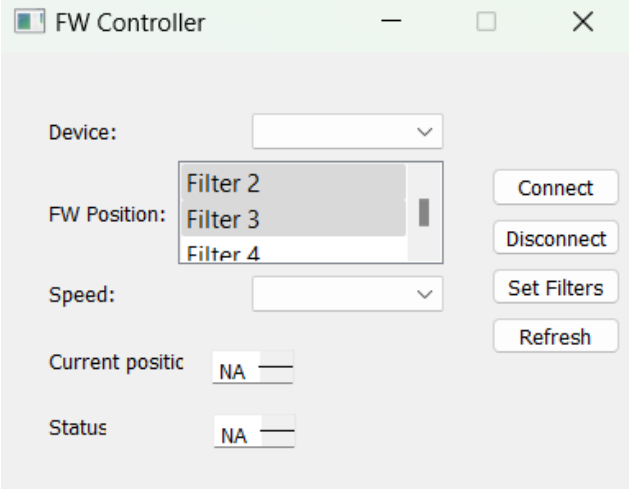

Figure 3.1 Graphical user interface (GUI) developed for filter wheel (FW) control. The interface allows users to select the device, choose filter positions, adjust the speed, and monitor the connection status and current position in real time. This tool was implemented using PyQt5 and PyVISA to automate filter control within the Raman imaging system.

Architecture

The interface was built with PyQt5, using the `Qt Designer` tool to create a layout consisting of device connection controls, filter position, selectors, and status monitors.

Features

The GUI automatically detects the available VISA resources (e.g., `ASRL5::INSTR`) and allows the user to select the appropriate port for the filter wheel. Users establish and close connection using the `Connect` and `Disconnect` buttons, respectively. Upon successful connection, the communication parameters (baud rate, data bits, stop bits, parity, etc.) were configured according to the manufacturer's specifications. The GUI provides a multi-selection list widget, where users can select multiple filter positions (e.g., Filter 1 through Filter 9). In the selection process, commands were sent sequentially to change the position of the filter wheel. For each selected filter, a position command was sent using the `PyVISA` interface, and the system optionally verified the position by querying the device. The current position and device status are updated in real time using two read-only text fields.

Implementation Details

Communication with the filter wheel was performed through a serial interface using PyVISA. The following command structure was used:

- `<position_number>`: Sends a command to move to the specified filter position.
- `GET_POSITION?`: Queries the current position of the filter wheel.

A short delay (10 ms) was introduced between consecutive commands to ensure that the filter wheel had sufficient time to respond before the next command was issued.

Example Workflow

When a user selects filters 2, 4, and 6, the following sequence is obtained:

1. The system sends "2" to the device.
2. A 10 ms pause ensures processing.
3. The system queries `GET_POSITION?` to verify the current position of the vehicle.

4. Steps 1–3 are repeated for filters 4 and 6.

This modular and responsive tool simplifies filter control during experimental acquisitions and integrates into a broader imaging workflow.

3.2.2 Collection and Detection Path

The system includes a set of four achromatic doublet lenses arranged in two imaging paths: the collection and detection paths. Each path includes one 200 mm and one 175 mm focal length doublet positioned close together (approximately zero spacing), forming a relay system with a total magnification of approximately $\frac{13}{17} \approx 0.76$. This configuration enables the demagnification of the 17×17 mm^2 field of view on the sample to a 13×13 mm^2 image on the CCD sensor, matching the active area of the 1024 $times$1024 Andor iKon-M camera with 13 μm pixel size. An important design choice is placing the filter wheel between the two lens groups at a location known as the pupil plane optically linked to the back aperture of the objective lens. By placing the filters here, we ensure that spectral filtering is applied evenly across the entire image, so every part of the field of view is treated the same way. Each band pass filter had a bandwidth of 0.8 nm and was used to isolate specific Raman bands (e.g., 1004 cm^{-1} or 1440 cm^{-1}). The optical layout was further optimized to minimize aberrations. All lenses were coated for near-infrared transmission to match the detection range (850–890 nm), and the optical axis was aligned with a reflective collimation path from the dichroic mirror. The collected light was passed through a 785 nm notch filter (33 nm bandwidth) to suppress elastic Rayleigh scattering before reaching the camera.

3.2.3 Illumination Path

The system was equipped with a fiber-coupled 785-nm diode laser, which safely and efficiently delivered laser light into the wide-field Raman imaging setup. The laser output was coupled into a 600 µm core diameter multi mode optical fiber (SMA–SMA), with a numerical aperture (NA) of 0.5. At the end of the fiber, the beam was collimated using a Thorlabs F810SMA-780 collimation package. This package included a plano-convex lens with a 36.02 mm focal length, aligned at 780 nm. To shape the beam and control its divergence, a diverging lens was placed immediately after the collimator. This expanded the beam diameter to better match the field of view required at the sample plane while maintaining uniformity. Following the divergent lens, a narrow band laser line filter (band pass) centered at 785 nm with a full width of 2–3 nm at half-maximum (FWHM) was inserted to ensure high spectral purity by suppressing the amplified spontaneous emission (ASE) and side modes of the laser. The collimated

and spectrally filtered beam was then directed toward the sample using a dichroic mirror positioned at a 45° angle. The dichroic mirror was designed to reflect the excitation light downward onto the sample while transmitting the back-scattered Raman signal returning from the sample. This epi-illumination geometry enables both illumination and collection to occur along the same optical axis. Figure 3.2 shows a schematic of the different optical components of the Multi-Spectral System.

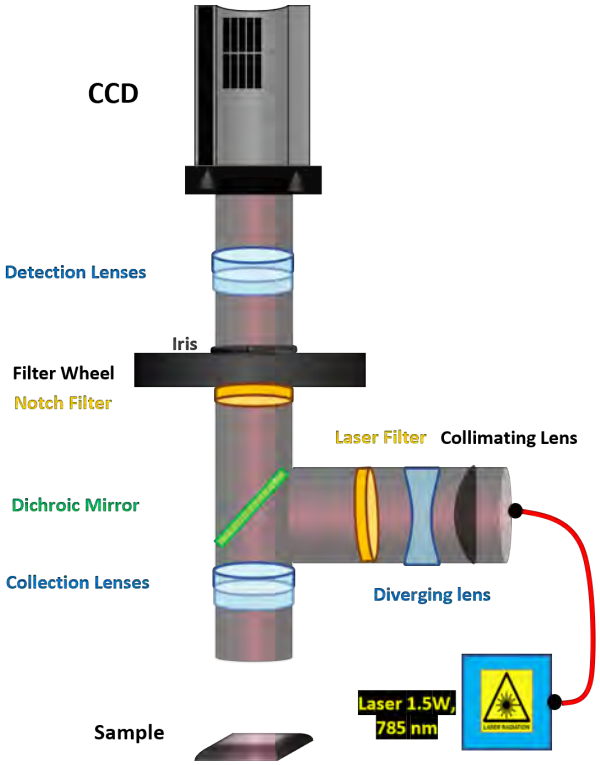

Figure 3.2 Schematic illustration of the wide-field Raman imaging system. The 785 nm laser (right) was fiber-coupled into a collimation package, diverging lens, and laser line filter. The beam was reflected by a dichroic mirror and focused onto the sample through collection lenses. The back-scattered Raman signals pass through the dichroic, notch, band-pass filters in the filter wheel, and detection lenses before reaching the CCD camera. The filter wheel is positioned in the pupil plane between the detection lens pair to enable multi spectral imaging.

3.3 Spectral and Spatial Resolution Characterization

3.3.1 Spatial Resolution Measurement Using USAF Target

To determine the spatial resolution experimentally, a standard 1951 United States Air Force (USAF) resolution test was imaged under white-light illumination using the same optical configuration as that of the Raman acquisition path. The USAF target contains groups of

line pairs at progressively smaller spacings, enabling the visual estimation of the smallest resolvable feature size. The system field of view was consistent with the Raman acquisition (approximately $17 \times 17\,\text{mm}$), and the image was captured using a CCD detector without Raman filtering to maximize the contrast. The smallest group and element in which both vertical and horizontal lines could be distinctly resolved were used to determine spatial resolution. The resolution limit was calculated using the known physical spacing of the elements on the USAF target. For the multi spectral system, the smallest resolved element corresponded to a line pair spacing of 350µm, confirming that the spatial resolution of the system met the design goal for wide-field Raman imaging applications.

3.3.2 Spectral Resolution

The spectral resolution of the system is determined by the bandwidth of the narrow band filters in the detection path. Each band pass filter had a full width at half maximum (FWHM) of 0.8 nm, which corresponds to approximately 10.2 cm^{-1} Raman resolution at 885 nm (corresponding to a 1440 cm^{-1} Raman shift). The following equation was used to convert the wavelength bandwidth to the Raman shift resolution:

$$\Delta\nu = \frac{10^7 \cdot \Delta\lambda}{\lambda^2}$$

The table below shows the spectral resolution for different band pass filters used for 1440 cm^{-1} band detection.

Table 3.2 Detection Wavelengths and Spectral Resolution for Filters Used Near 1440 cm^{-1}

Raman Shift (cm^{-1})	**Detection Wavelength (nm)**	**Spectral Resolution (cm^{-1})**
1375	881.4	10.30
1407	883.2	10.26
1440	885.0	10.20
1462	886.3	10.17
1490	887.7	10.15

3.4 Noise Sources and Mitigation Strategies

Reliable detection of weak Raman signals requires a deep understanding of the noise sources that affect the image quality. These noise sources can be classified as electronic, thermal, optical, and environmental, each contributing differently to the overall signal-to-noise ratio

(SNR) of the system [33, 45, 46]. In the following section, I briefly explain each type of noise and its effects on image acquisition.

3.4.1 Readout and Electronic Noise

Readout noise arises from charge-to-voltage conversion and analog-to-digital processing in CCD electronics. This noise is independent of the signal level and sets the baseline noise of the detector. For the iKon-M 934 camera, the read noise varies from **2.9 e^-** at 0.05 MHz to **18 e^-** at 5 MHz, depending on the selected pixel readout rate [46]. This trade-off between speed and noise is typical of CCD-based systems; lower readout speeds are preferred when imaging weak Raman signals, especially under low-light conditions.

3.4.2 Dark Current and Thermal Noise

Thermal noise results from thermally generated electrons within the CCD sensor, which contribute to the overall background signal during prolonged exposure. This noise is particularly problematic for low-light applications such as Raman imaging. The iKon-M 934 deals with this by deep thermoelectric cooling (down to **-60°C**), reducing the dark current to as low as **0.00012 e^-/pixel/s** [46]. This is essential for maintaining a low background noise during long integration periods, especially for weak Raman scattering from biological tissues.

3.4.3 Photon Shot Noise

Photon shot noise is an inherent statistical fluctuation in photon arrival that follows a Poisson distribution. It is proportional to the square root of the signal ($\sqrt{N}$) and is unavoidable in photon-limited imaging systems. Unlike readout or dark noise, it cannot be removed by hardware design but can be minimized by averaging multiple frames, increasing the integration time (within safety and saturation), and enhancing signal strength through optical design and exposure optimization [45].

3.4.4 Interference Effects: Scattering Artifacts and Etaloning

Multiple scattering within the tissue can blur spatial features and decrease the specificity of the Raman signal. Additionally, thin-film interference within CCD sensors (etaloning) causes unwanted fringe patterns, particularly in the near-infrared (NIR) range. The iKon-M 934 camera uses the BEX2-DD sensor with **Fringe Suppression Technology™** to reduce etaloning in the 850–900 nm range, which aligns with the key Raman bands (e.g., 1004 cm^{-1} and 1440 cm^{-1}) [46].

3.4.5 Environmental and Systemic Noise

External noise sources include ambient light from the room, vibrations from nearby instruments, and electromagnetic interference (EMI) from power lines and motors. To reduce these influences:

- The system operates in a darkened enclosure with minimal ambient light.
- All optical components are mounted on a vibration-isolated optical table.
- Shielded cables and grounding are used to prevent EMI from affecting the CCD electronics.

Such conditions are necessary in optical imaging systems to protect the low-noise performance of sensitive detectors [33, 45].

3.4.6 SNR System Sensitivity

To report detector-limited sensitivity consistently, we compute the SNR in the raw domain including both photon (shot) noise and read noise. In electron units,

$$\mathrm{SNR} = \frac{S_{e^-}}{\sqrt{S_{e^-} + R^2}}, \quad S_{e^-} = g\,(\mu_{\mathrm{sig}} - \mu_{\mathrm{dark}}),$$

where g is the camera gain (e^-/ADU), R is the read noise (e^- rms), and $\mu_{\mathrm{sig}}, \mu_{\mathrm{dark}}$ are mean raw counts (ADU) in the same ROI. Equivalently, in ADU the denominator combines shot noise and read noise:

$$\mathrm{SNR} = \frac{\mu_{\mathrm{sig}} - \mu_{\mathrm{dark}}}{\sqrt{\frac{\mu_{\mathrm{sig}} - \mu_{\mathrm{dark}}}{g} + \sigma^2_{\mathrm{dark}}}},$$

with σ_{dark} the temporal standard deviation measured from dark frames (ADU). Using this formulation avoids overestimation in the shot-noise regime and reconciles the empirical and theoretical SNR calculations.

Table 3.3 System performance summary

Parameter	**Experimental value**	**Unit / condition**	**Notes**
Spatial resolution (USAF target)	350	μm	From prior calibration (Section 3.3.1)
Spectral resolution	10–12	nm ($\approx$130 cm^{-1})	Estimated from filter bandwidths
Read noise	2.9–18	e$^-$ rms	Camera spec @ 1–3 MHz readout
Read noise (3 MHz mode)	$\approx$12	e$^-$ rms	Measured from dark frames
Gain	3	e$^-$/ADU	Camera setting during acquisition
Signal level (S_{e^-})	3×10^4	e$^-$ pixel^{-1}	Typical bright calibration ROI
SNR	$\approx$184	—	Raw frames, dim sample region
SNR (bright calibration, 10-frame average)	$\approx$550	—	$\sqrt{M}$ improvement ($M = 10$)

CHAPTER 4 PRECLINICAL EVALUATION

4.1 Chapter Overview

This chapter descries the acquisition and processing pipeline that we used to evaluate the multi spectral Raman imaging system on biological tissues. The focus was on differentiating fat and muscle tissue based on the Raman band at $1440\,\mathrm{cm}^{-1}$, associated with CH_2 bending vibrations. The methodology included sample preparation, laser exposure control, and multi spectral image acquisition across selected spectral bands. Spatial deformities were corrected using a Spectralon, and the spectral variations were addressed using an NIST-traceable Raman standard. Subsequent processing steps involve dark subtraction, spectral mapping, and fluorescence background removal using baseline correction algorithms. Final Raman maps were generated from baseline-subtracted spectra, and multiple filter combinations were compared to identify the optimal spectral windows for contrast enhancement. This experimental framework serves as the foundation for the next chapter, in which the same strategy is applied to brain tissue samples containing both cancerous and normal regions of interest.

4.2 Sample Preparation and Acquisition Protocol

To evaluate the performance of the multi-spectral imaging system, fresh meat chops consisting of both muscle and fat tissues were used as representative biological samples. These tissues were selected because of their strong biochemical contrast: muscle is protein-rich, whereas fat has distinct lipid-related Raman characteristics, making them suitable for assessing system sensitivity and spectral contrast in the 1440 cm^{-1} region. In addition, Spectralon and a certified NIST Raman standard were used for spatial correction and intensity calibration. The Raman spectra of the fat and muscle tissues are shown in Figure 4.1, highlighting the clear differences in peak intensities.

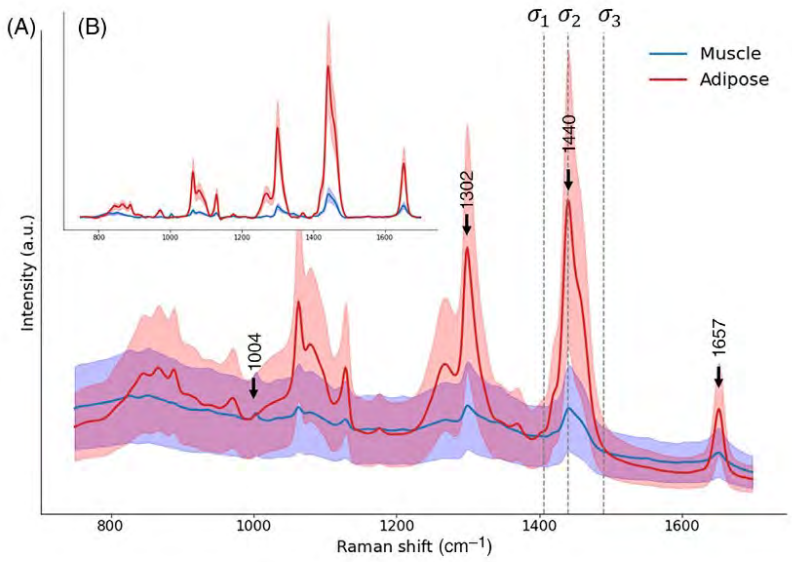

Figure 4.1 Raman spectra of adipose and muscle tissues captured using the hyperspectral imaging system: (A) Mean raw spectra with corresponding variance across the field of view. (B) Processed spectra following background subtraction, showing reduced variability in the spectra. The vertical dashed lines in (A) indicate the three spectral bands selected for the multi-spectral system, centered at Raman shifts of 1407, 1440, and 1492 cm^{-1}. Reprinted from [25] with permission.

4.2.1 Sample Preparation: Biological Tissue

Fresh pork and beef chops were purchased from a local butcher, dried, and cut into a flat surface to ensure a consistent focus in the field of view. The size of the samples was between 2-4 cm^2, with a thickness of 1–2 cm. Each sample was mounted on a matte black substrate to reduce reflections and immobilized with non-fluorescent tape.

4.2.2 Laser Exposure and Illumination Area

A 785 nm fiber-coupled diode laser was used as the excitation source, delivering the highest power of 550 mW at the sample plane. The laser beam was collimated and expanded using a diverging lens and filtered through a 785 nm band pass filter before being directed onto the sample via a 45 ° dichroic mirror. The field of view was approximately 17×17 mm^2 (2.89 cm^2), resulting in an average irradiance of

$$\text{Irradiance} = \frac{550 \text{ mW}}{2.89 \text{ cm}^2} \approx 190 \text{ mW/cm}^2$$

This irradiance level remained below the established thermal damage thresholds for short exposure durations (2–4 s). For near-infrared wavelengths, such as 785 nm, the thermal damage threshold for skin and soft tissues is typically in the range of 100–200 mW/cm^2 for exposure durations of a few seconds, with radiant exposures below 1–2 J/cm^2 considered safe to avoid irreversible tissue damage [47–49].

4.2.3 Multi-spectral Image Acquisition

I acquired the images of samples (adipose/muscle tissues) using five narrow-band filters centered at 1375, 1407, 1440, 1462, and 1490 cm^{-1}, each with a bandwidth of 0.8 nm. The filter wheel was automated and synchronized with the camera using PhysSpec software. For each band, 2–4 s exposures, and 5-frame averaging was used to improve the signal-to-noise ratio. A background (dark, with laser off) frame was also acquired and subtracted from each image to correct for the system noise.

4.2.4 Diffuse Reflectance Calibration Using Spectralon

To correct for spatial inhomogeneities in the illumination and system response, we used a Spectralon reflectance standard. Spectralon is a highly Lambertian material with over 99% reflectance in the near-infrared region and negligible inelastic scattering, making it ideal for optical calibration in Raman imaging systems. A reflectance image was acquired by

illuminating the Spectralon surface with a 785 nm laser and collecting the reflected light through a 785 nm bandpass filter.

4.2.5 Spectral Calibration with NIST Standard

A NIST-certified Raman calibration standard (SRM 2241 or equivalent) was used to validate the spectral accuracy. This standard contains a material with known Raman peaks (e.g., polystyrene or naphthalene), allowing for spectral alignment and wavenumber mapping. Calibration was performed by aligning the filter-based band assignments of the system with the known positions of the standard peaks, ensuring an accurate interpretation of the Raman shift between the filters.

4.3 Spectral Processing and Baseline Correction

To extract accurate Raman signal, we applied a multi-stage preprocessing pipeline: dark subtraction, reflectance correction with Spectralon, spectral correction with NIST, and background fluorescence subtraction. All data processing was performed using custom MATLAB scripts developed for batch-image handling and visualization.

4.3.1 Data Organization and Loading

Raw image cubes were stored in `.h5` format and loaded into MATLAB using the `h5read` function. A structure was created for each acquisition containing metadata such as sample type (e.g., pork, dark, NIST, Spectralon), filter number, exposure time, and laser voltage. The images were then averaged across the time frames to improve the signal stability and reduce the temporal noise.

4.3.2 Dark Signal Removal

Each sample image was paired with a dark frame acquired under identical filter and exposure conditions but with the laser off. The dark image was subtracted pixel-wise from the sample images. The negative values were clipped to zero.

4.3.3 Diffuse Reflectance Calibration Using Spectralon

Because the Spectralon and tissue sample acquisitions used the different laser powers and integration times, was applied a scaling factor S to normalize the intensity.

$$S = \frac{P_{\text{sample}} \cdot t_{\text{sample}}}{P_{\text{spectralon}} \cdot t_{\text{spectralon}}}, \tag{4.1}$$

where P is the laser power, and t is the integration time for the respective acquisitions.

The tissue sample image was divided pixel-by-pixel by the corresponding Spectralon image to remove the system-induced spatial deformities. The resulting image was then multiplied by the scaling factor S to ensure that the corrected Raman intensity remained quantitatively accurate. This reflectance-based correction significantly improved the spatial uniformity of the Raman signal and the interoperability of biochemical features across the field of view.

4.3.4 Spectral Correction Using NIST Standard

To correct for the system spectral response, we used images of an NIST-certified Raman reference material. The average signal from the NIST sample was normalized and used as a per-filter-scaling factor. Additionally, a fifth-order polynomial calibration curve was fitted to map the Raman shift to the filter center wavelength for improved accuracy in band assignment:

$$\text{Wavelength} = A_0 + A_1\nu + A_2\nu^2 + A_3\nu^3 + A_4\nu^4 + A_5\nu^5$$

4.3.5 Fluorescence Background Subtraction and Baseline Correction

Because biological samples such as fat and muscle has auto fluorescence, further background subtraction was applied. Raman images corresponding to 1440 cm^{-1} were corrected using baseline estimates obtained from neighboring bands (e.g., 1407 and 1462 cm^{-1}) via linear interpolation:

$$I_{\text{baseline}} = a \cdot \nu + b$$

$$I_{\text{Raman}} = I_{1440} - I_{\text{baseline}}$$

Multiple correction schemes were tested using different filter pairs (e.g., 1375 and 1490 or 1407 and 1490), and the resulting Raman images were normalized and visualized using color-mapped intensity plots.

4.3.6 Baseline Algorithms Used

Baseline correction is an essential step in processing of the Raman data, particularly for biological samples, where strong auto fluorescence can obscure weak inelastic scattering. Several algorithms exist for baseline removal, each with strengths and limitations depending

on the nature of the background and target Raman peaks. Traditional numerical baseline correction methods such as, **Polynomial fitting** (e.g., iModPoly, ModPoly), fits low-order polynomials to estimate smooth baseline trends.**Morphological operators** (e.g., MorphBR) also apply filters based on signal shape to estimate background. Furthermore, a more recent method, **BubbleFill**, fills the baseline regions using a convex hull-based approach, which is particularly robust for sharp Raman peaks over broad fluorescence backgrounds. Although these methods work effectively on full spectra, they are not directly applicable to multi spectral Raman imaging systems, where only a few discrete Raman bands are imaged rather than the entire spectrum.

Baseline Subtraction in Multi-spectral Imaging In this study, a baseline subtraction approach specifically tailored to the constraints of a filter-based imaging system was used. We applied the method used by David et al. (2024) [25]. In this method, the images at Raman shifts neighboring the target band (1440 cm^{-1}) are used to estimate and subtract the fluorescence background. The method assumes that the off-band filters (e.g., 1407 and 1490 cm^{-1}) capture primarily fluorescence and a negligible Raman signal. A linear interpolation between these off-band images estimates the fluorescence baseline at the Raman band at 1440 cm^{-1} as follows:

$$I_{\text{baseline}}(x, y) = \frac{I_{1407}(x, y) + I_{1490}(x, y)}{2}$$

$$I_{\text{Raman}}(x, y) = I_{1440}(x, y) - I_{\text{baseline}}(x, y)$$

This approach allows for recovery of the true contribution of inelastic scattering at 1440 cm^{-1} without requiring full spectral data. Variations of this method were also applied using other filter combinations, such as (1375, 1490) and (1407, 1462), and linear interpolation was used to model the fluorescence background. This model-free subtraction strategy enables fast, wide-field imaging of specific Raman biomarkers and shows promise for intraoperative implementation due to its simplicity and computational efficiency.

4.3.7 Raman Band Selection and Correction Schemes

To isolate the 1440 cm^{-1} Raman contribution, we used the spectral subtraction strategy described in Section 4.3.6. Specifically, a combination of off-band filter images was used to estimate and remove the fluorescence background. The following filter pairs were tested.

- (1407, 1462) — centered symmetrically around 1440 cm^{-1}, see figure 4.2c.

- (1375, 1490) — broader spectral range, more robust to slow fluorescence drift, see figure 4.2b.
- (1407, 1490) and (1375, 1462) — alternative asymmetric models, see figure 4.2a and 4.2d, respectively.

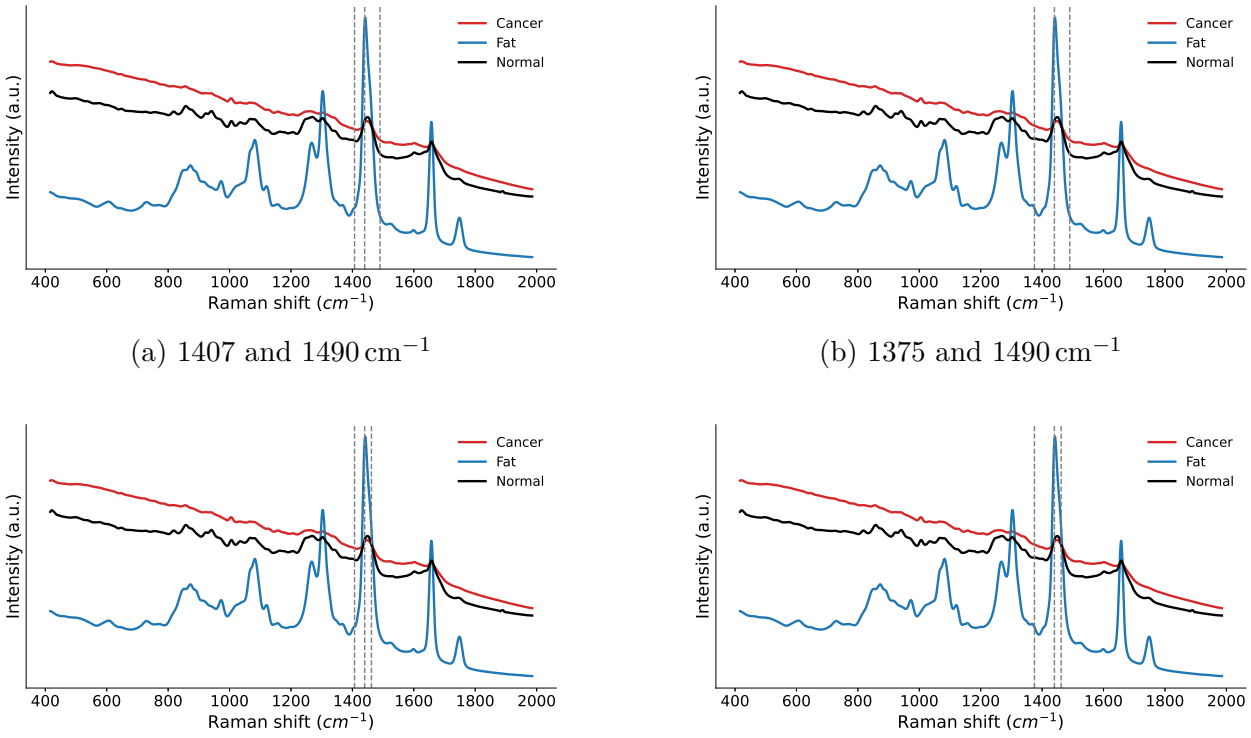

(a) 1407 and 1490 cm^{-1}

(b) 1375 and 1490 cm^{-1}

(c) 1407 and 1462 cm^{-1}

(d) 1375 and 1462 cm^{-1}

Figure 4.2 Spectra of different tissue types; normal, cancer, and fat with the placement of different filter pairs around the 1440 cm^{-1} band. Vertical dashed lines indicate filter centers used for linear interpolation-based baseline correction.

4.4 Processed Imaging Results: Fat vs. Muscle

This section presents the final Raman imaging results from the pork tissues(muscle and fat regions). Following the complete preprocessing pipeline, including dark signal subtraction, spatial normalization using Spectraoln, spectral correction with a NIST standard, and fluorescence background subtraction, Raman contrast maps were generated for the 1440 cm^{-1} band, which is sensitive to lipid and protein content.

4.4.1 Multispectral Raw Raman Images (Preprocessed)

Multi-spectral Raman imaging was performed using five narrow band filters centered at Raman shifts of 1375, 1407, 1440, 1462, and 1490 cm^{-1}. Each filter selectively captures Raman + auto fluorescence photons in a narrow spectral window (0.8 nm FWHM), allowing the sampling of different vibrational bands in the tissue. Raw Raman images were acquired using a CCD camera with consistent exposure and laser power for each filter. Each acquisition generated a hyperspectral cube, and the first processing step involved averaging all the frames per filter to reduce the temporal noise. No background or correction was applied during this stage. Figure 4.3 shows the five averaged raw Raman images for a representative tissue sample, without dark subtraction or calibration. Spatial variations in illumination and signal intensity are visible, which are addressed in subsequent correction steps.

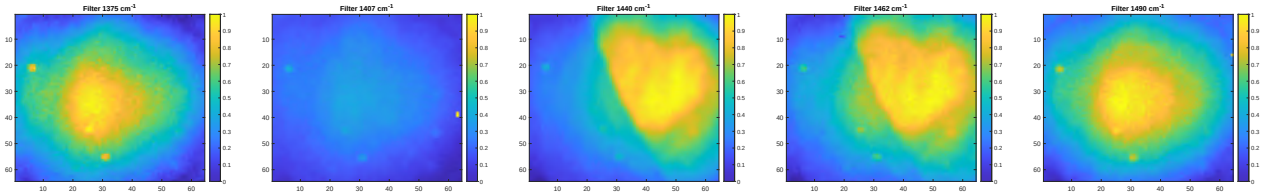

(a) 1375 cm^{-1} (b) 1407 cm^{-1} (c) 1440 cm^{-1} (d) 1462 cm^{-1} (e) 1490 cm^{-1}

Figure 4.3 Raman images captured using five narrow band filters targeting specific Raman shifts around the 1440 cm^{-1} band. Each image represents one acquisition band before baseline subtraction.

Reflectance-Based Correction Using Spectralon The sample images acquired with each filter were corrected by dividing each pixel by the corresponding pixel of the Spectralon reference.

$$I_{\text{corrected}}(x, y) = \frac{I_{\text{sample}}(x, y)}{I_{\text{Spectralon}}(x, y) \cdot S} \tag{4.2}$$

Here, S is a scaling factor used to adjust for differences in acquisition parameters, such as laser power or integration time, between the reference and sample images. This factor ensured that the corrected image retained its relative intensity profile while being quantitatively comparable.

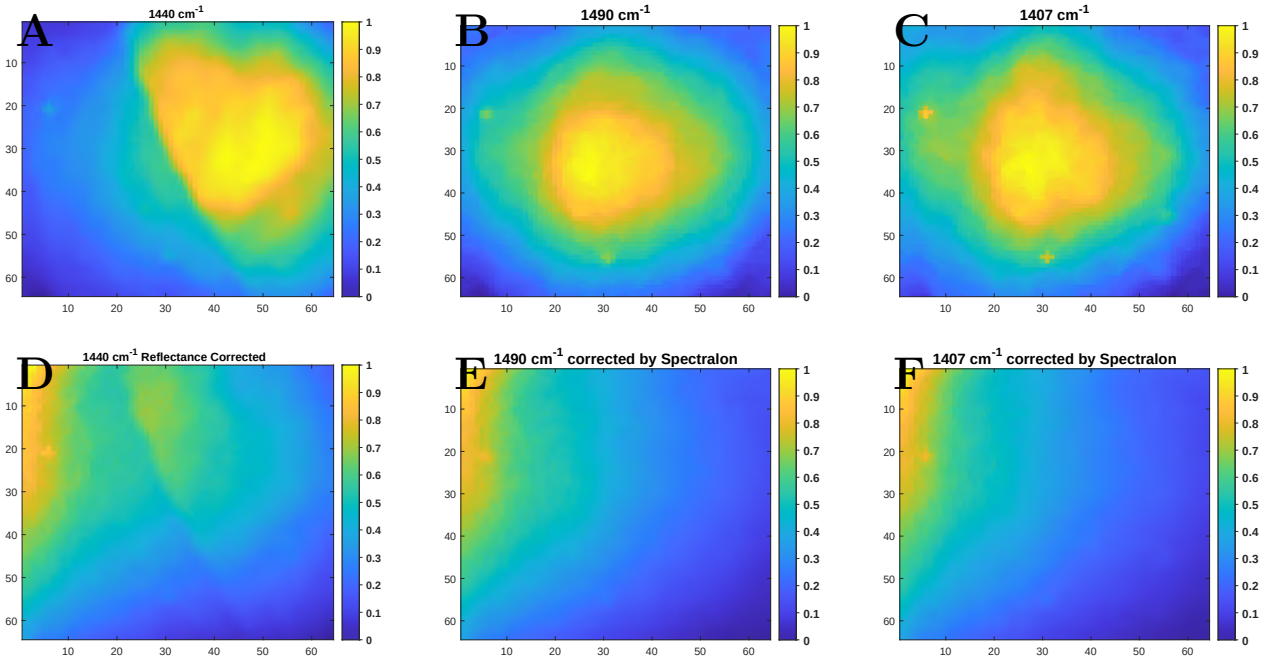

Figure 4.4 A, B, and C: Images of different filter before correcting by spectralon. D, E, F: Images of the filters after correction by Spectralon.

Spectral Response Correction using NIST-Traceable Reference To compensate for the wavelength-dependent variations in system sensitivity (filter transmission, detector efficiency), an NIST-traceable Raman standard (e.g., SRM 2241) was used. This material has a well-characterized Raman peaks across a wide spectral range, allowing for relative sensitivity normalization between the spectral channels.

For each filter, the average intensity of a known reference peak from the standard was calculated and used as a multiplicative correction factor. This ensured that the relative spectral response across all channels was normalized, allowing for a consistent quantitative comparison.

Furthermore, a fifth-order polynomial function was fitted to the known Raman shifts of the reference peaks to accurately map the pixel indices to the Raman wavenumbers. This spectral mapping ensures proper alignment across the spectral bands, which is essential for combining multi spectral data into a coherent Raman image.

Together, these corrections, spatial response normalization using spectralon, and spectral

response correction using an NIST standard enabled accurate baseline subtraction and reliable tissue contrast analysis. Figure 4.5 shows representative images before and after the corrections.

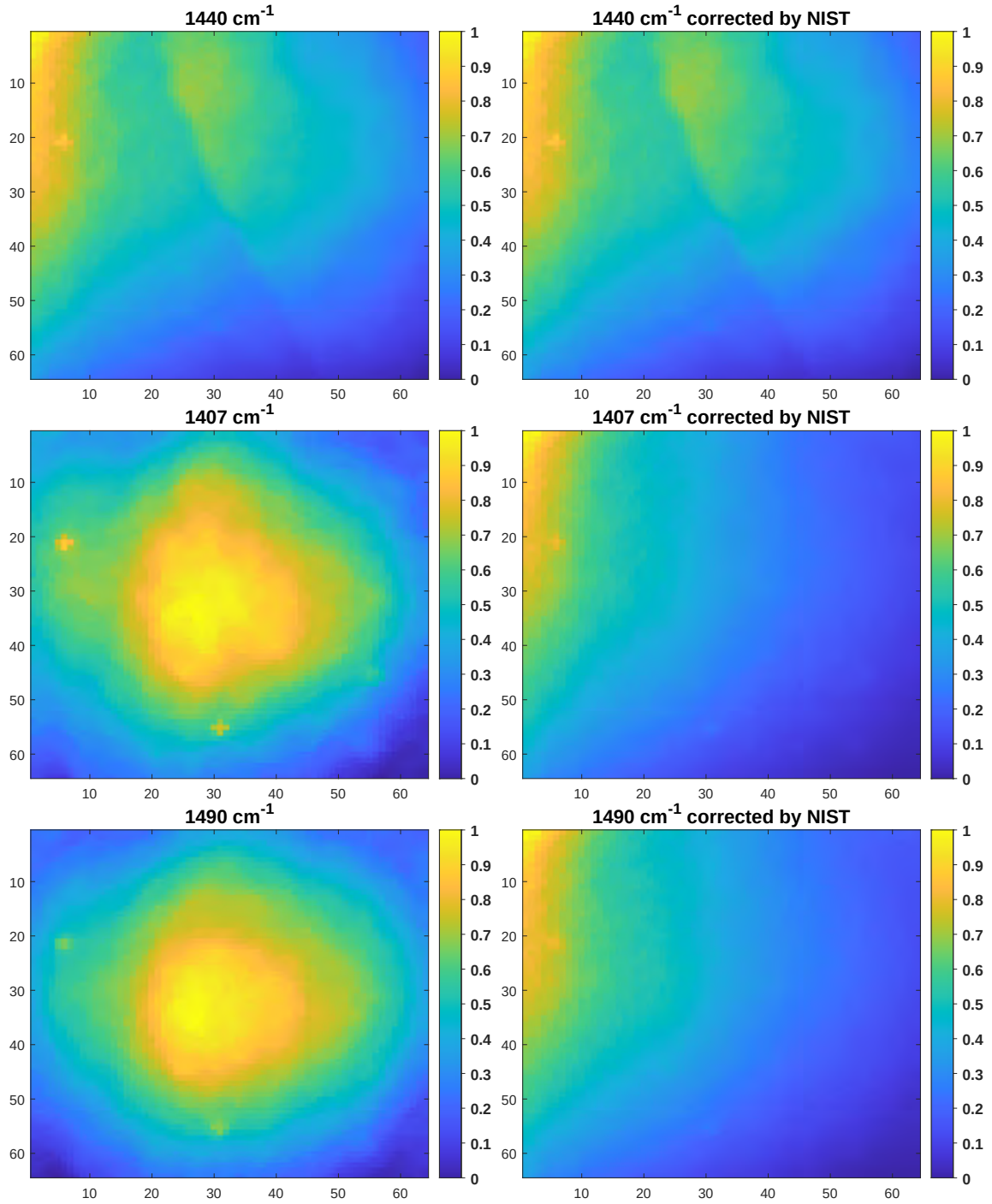

Figure 4.5 Image acquired with the band pass filter at 1440 cm^{-1}, before (left) and after (right) correcting by NIST.

4.4.2 Baseline Subtracted Raman Maps at 1440 cm^{-1}

After system response normalization and baseline correction, we generated Raman intensity maps centered at 1440 cm^{-1} using different filter pairs. Due to the narrow-band detection approach used in the multi spectral system, multiple band pass filters centered around the 1440 cm^{-1} shift were employed to ensure robust capture of the Raman signal while minimizing spectral overlap and background interference. For each filter pair, a baseline-subtracted Raman image was extracted, normalized, and compared visually. Figure 4.6 displays the resulting 1440cm^{-1} Raman maps obtained with different filter combinations. While all filter pairs target the same Raman band, subtle differences in intensity and contrast are visible, reflecting the influence of the spectral bandwidth, filter alignment, and possible residual fluorescence.

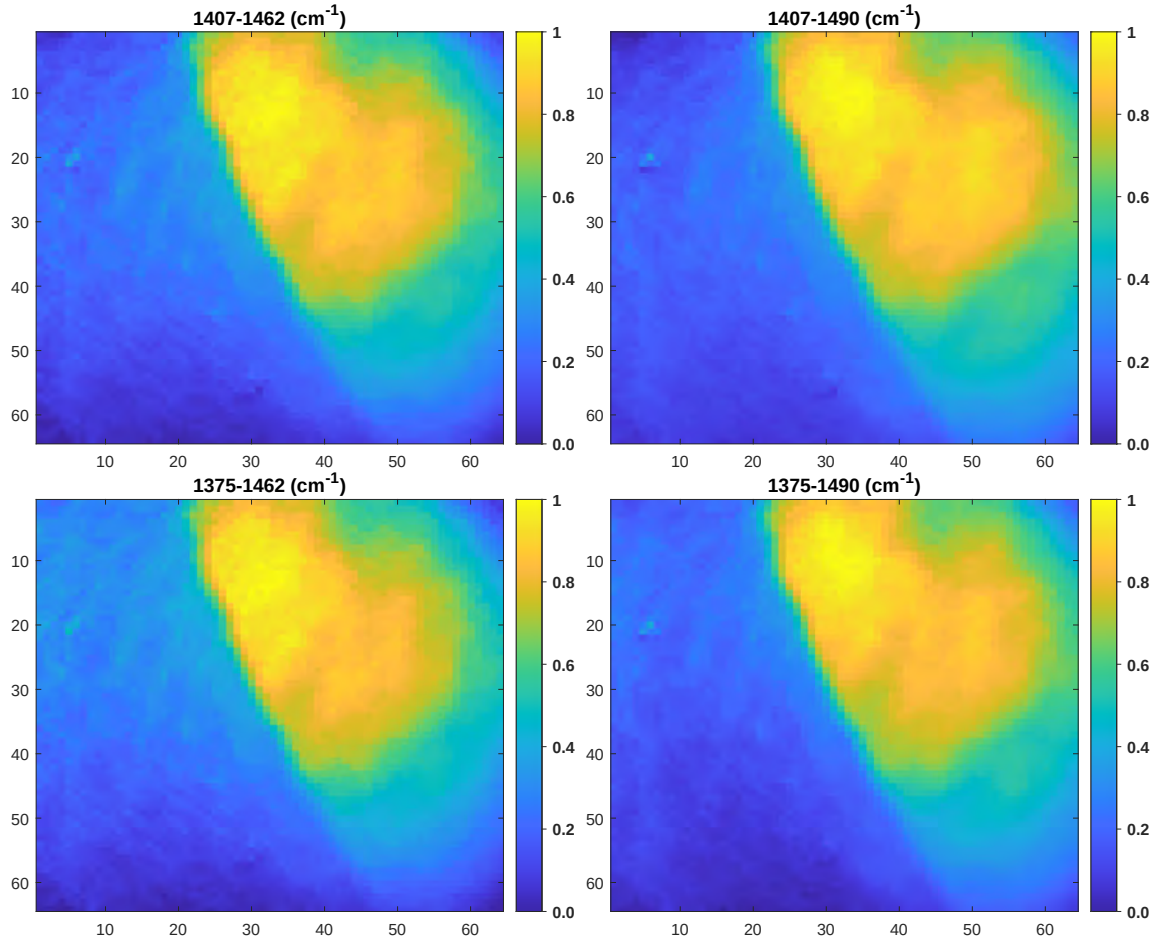

Figure 4.6 Baseline-corrected Raman images at 1440 cm^{-1} using different filter pairs for fluorescence estimation. Top left: 1407–1462; top right: 1375–1490; bottom left: 1407–1490; bottom right: 1375–1462.

4.4.3 Quantitative Comparison

To compare filter combinations, intensity histograms were obtained from manually selected regions corresponding to the fat and muscle tissues. This comparison enables evaluation of the contrast and separation achieved between the two tissue types for each filter pair targeting the 1440 cm^{-1} Raman band. Figure 4.7 presents the normalized intensity distributions for each set of filters, highlighting the degree of overlap or separation between the Raman signals associated with fat and muscle. Filter combinations that produce well-separated histograms with minimal overlap are considered more effective in isolating the 1440 cm^{-1} signal and enhancing tissue contrast. Among the filter combinations evaluated, the pair that spanned 1407–1490 cm^{-1} demonstrated the best performance in separating fat and muscle signals. As shown in the upper left of Figure 4.7, the corresponding histogram displays two well-separated peaks with minimal overlap, reflecting a high contrast between the lipid- and protein-rich regions. In contrast, wider spectral windows, such as 1375–1490 cm^{-1} and 1375–1462 cm^{-1} show broader, overlapping distributions, reducing their discriminative power. Based on this analysis, the 1407–1490 cm^{-1} filter pair was selected as the optimal spectral window for targeting the CH_2 bending mode at 1440 cm^{-1} in the final Raman imaging analysis for adipose muscle tissues.

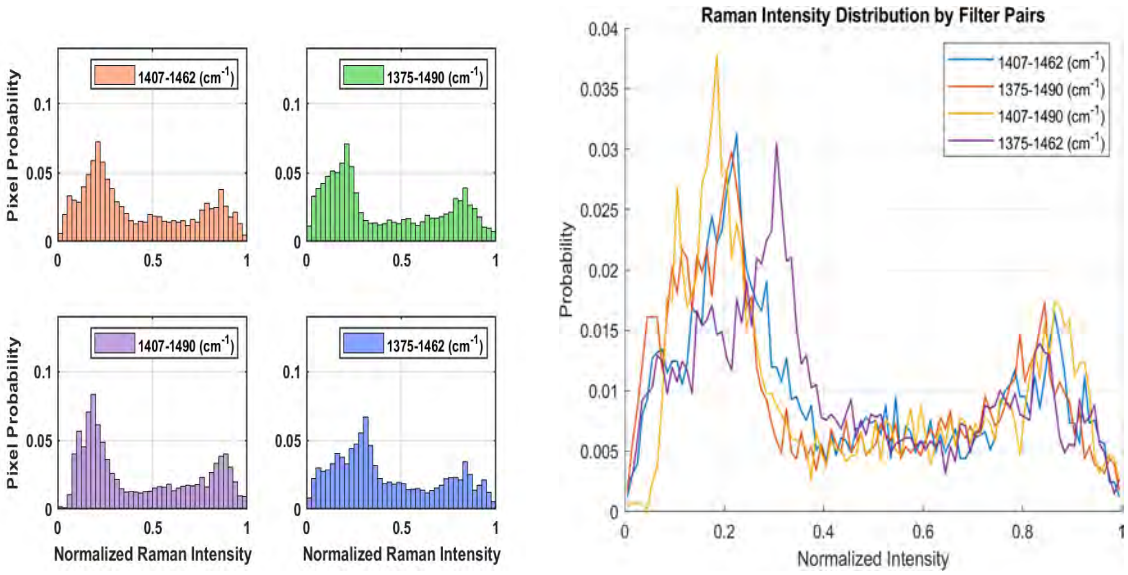

Figure 4.7 Pixel intensity histograms of final Raman Images at 1440 cm^{-1} for different filter Pairs

4.4.4 Conclusion, and Final Results

Histogram analysis of the normalized Raman intensity distributions (Figure 4.7) validates the baseline subtraction strategy for fat/muscle differentiation. This method significantly enhances the contrast even in the presence of broad auto fluorescence, with the (1407, 1490) cm^{-1} filter pair demonstrating the most distinct separation between fat and muscle. In addition to spectral validation, visual inspection of spatially resolved maps confirmed the robust classification capability. Figure 4.8 presents the final outputs for a representative tissue sample, including a cellphone photograph to observe the fat and muscle parts of the sample, a bright-field reference showing the image taken without any filter and serving to observe the fat/muscle margins, corrected Raman intensity map, and resulting classification. These results illustrate the successful mapping of the targeted band at 1440 cm^{-1} using (1407, 1490)cm^{-1} filter pairs.

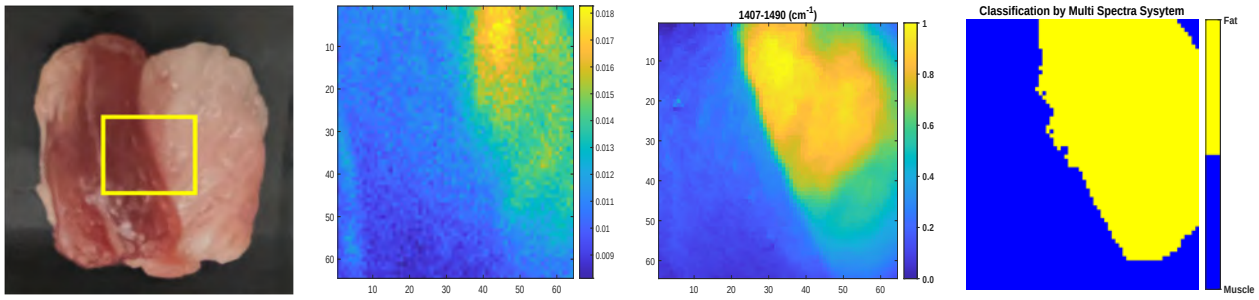

(a) Cellphone photo (b) Bright-field image (c) Raman map (d) Classification map

Figure 4.8 Overview of the fat and muscle tissue sample. (a) Mobile phone image of the tissue, (b) Bright-field image showing orientation, (c) Raman intensity distribution at 1440 cm^{-1}, and (d) Tissue classification map distinguishing fat and muscle.

The simplicity and computational efficiency of this baseline subtraction and filter-pair strategy make it highly promising for real-time surgical applications. In the next chapter, we extend the method to human brain tumor samples, to evaluate tumor detection.

CHAPTER 5 CLINICAL APPLICATION AND TESTING

To validate the practicality of the multi spectral Raman imaging system, a series of ex vivo tests was conducted on cancerous brain tissues. This chapter presents the implementation of the system for this study, including the setup process, clinical imaging protocol,and the image and data processing. Preliminary results from four patients are reported to assess the system performance, followed by a discussion of the challenges encountered during intraoperative usage.

5.1 Surgical Environment Setup

The multi spectral system was initially assembled on a movable optical breadboard to ensure the mechanical stability of the optical components. The setup was then mounted on a cart, allowing the entire system to be securely transported to the neurology department. Montreal Neurological Institute-Hospital(MNI) while maintaining precise optical alignment. The control software, PHySpecTM, was installed on a laptop to ensure full control over the camera and motorized filter wheel during ex vivo measurements at the MNI. The figure shows the final setup for the ex vivo study at the MNI.

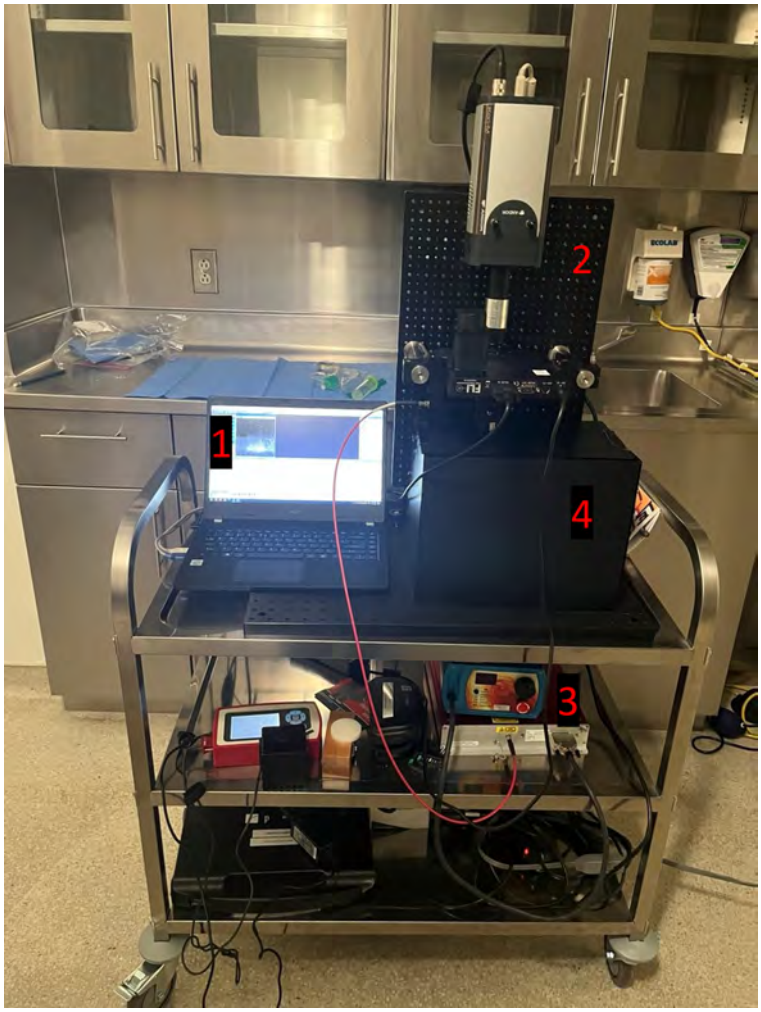

Figure 5.1 Experimental setup of the multi-spectral Raman imaging system configured for ex vivo measurements. The system includes a laptop (1) for control, the multi spectral system (2), the laser (3), the black chamber for putting the sample inside (4), and supporting electronics on the lower shelves.

5.2 Specimen Preparation and Histology Alignment

A standardized procedure was established for the collection and preparation of the brain tissue. The samples were typically between 1 and 4 cm^3. Each sample was immediately immersed in phosphate-buffered saline (PBS; Thermo Scientific, 312–651, USA) and transferred to a sterile petri dish. Using a sterile razor blade, the samples were sectioned into two smaller flat samples approximately 10 mm $\times$ 10 mm $\times$ 3 mm in size. To minimize the background signal in the Raman spectra, each sample was placed on an aluminum surface (Miro5011, Anomet, Canada), which exhibits minimal inelastic scattering in the 400-2100 cm^{-1} range. Throughout the imaging session, PBS was periodically sprayed on the samples to prevent dehydration and to maintain the physiological temperature. Importantly, the buffer solution did not alter the Raman spectral signature of the tissue. Raman imaging was performed in the available surgical space near the patient. After imaging, a spatial registration procedure was implemented to align the Raman and white-light images with the histopathology data. The borders of the square tissue samples were marked using a three-step inking process: (1) all edges were treated with 5% acetic acid; (2) three sides were inked with different colors (top: red, right: green, bottom: blue); and (3) the ink was left to dry for five minutes. The samples were then transferred to micro-tissue cassettes and placed in fresh 10% paraformaldehyde for an additional 24 h before paraffin embedding. Serial sections were obtained from the top surface of each formalin-fixed, paraffin-embedded (FFPE) sample, covering the entire imaging area. The sections were stained with hematoxylin and eosin (H&E) and scanned to produce high-resolution digital images. As illustrated in Figure 5.2, the specimen preparation protocol involves sequential steps from tissue collection to histological analysis.

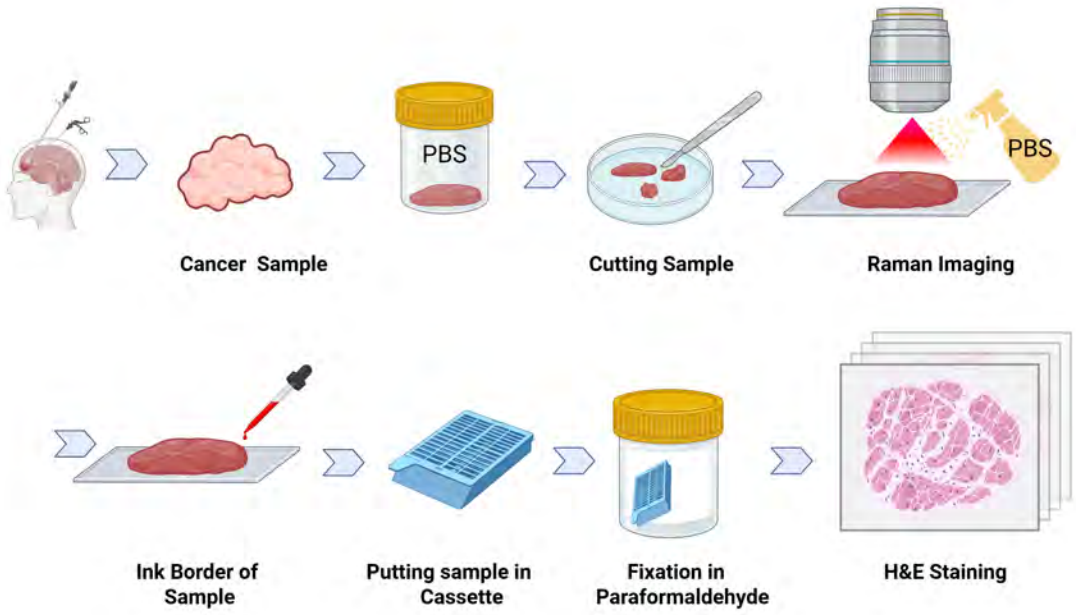

Figure 5.2 Step-by-step specimen preparation and histology alignment workflow. This includes tissue collection, PBS immersion, sample trimming, placement on aluminum backing, Raman imaging with PBS spraying to prevent dehydration, inking of tissue borders, cassette transfer, paraformaldehyde fixation, and final H&E staining for histological analysis.

5.3 Image acquisition process

Before Imaging , we ran calibrations with a NIST-traceable standard, Spectralon, and dark frames. These calibrations were done using all the band pass filters intended for sample acquisition and under identical imaging parameters (e.g., exposure time, laser power, and filter wheel configuration).

5.4 Image Processing Steps for brain data

All calibration steps applied to the brain, including dark subtraction, spectralon, and NIST, matched with those applied to the adipose/muscle data, as described in detail in the previous

section. However, the auto fluorescence/baseline subtraction differed for brain tissues.

Figure 5.3 shows the Raman spectra of glioblastoma and normal brain tissue adopted from a multi-center study [17]. In Ember *et al.* study, all spectral processing were performed using Python (v3.7.10) with the`scikit-learn` library (v1.0.2). Pre-processing routines were adapted from an open-source Raman spectroscopy analysis framework described by Sheehy *et al.* [13], which implements a validated baseline correction approach. Each Raman spectrum underwent a standardized pre-processing pipeline to ensure consistency across the dataset. First, a dark-count background spectrum acquired with the laser turned off was subtracted from each measurement. Cosmic ray artifacts were then identified and removed. Wavenumber calibration was performed using the known Raman peak positions of a polycarbonate reference sample, followed by instrument response correction using a NIST-traceable 785 nm Raman calibration standard. Also, to improve signal-to-noise ratio, 20 consecutive spectra acquired at the same spatial location were averaged. Baseline subtraction was subsequently performed using the BubbleFill algorithm [13], an iterative method that removes broad auto fluorescence background by growing virtual bubbles across the spectrum. The minimum bubble diameter was fixed at 60 cm^{-1}, corresponding approximately to the width of the lipid/protein Raman band near 1441 cm^{-1}. This parameter was selected to allow fully automated and unbiased processing of the entire dataset without user-dependent tuning. Following baseline correction, spectra were smoothed using a third-order Savitzky–Golay filter with a window size of 11 points and finally normalized using standard normal variate (SNV) normalization. This pre-processing strategy ensures reproducible extraction of Raman spectral features while minimizing the influence of auto fluorescence,instrumental variations, and inter-sample intensity fluctuations.

After all above spectral processing steps (see the bottom part of figure5.3), the Raman spectrum highlights the intensity difference at the 1440 cm^{-1} lipid/protein band in normal and Cancer tissues. This means that the Raman intensity of normal brain tissue at 1440cm^{-1} is higher than that of cancerous tissues.

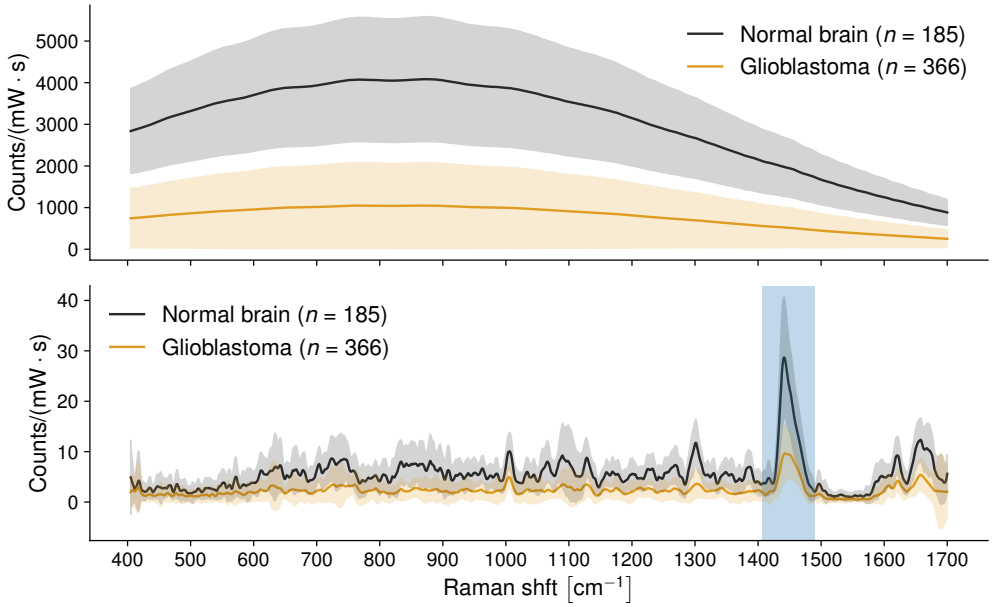

Figure 5.3 Mean Raman spectra of glioblastoma (orange, $n = 366$) and normal brain tissue (black, $n = 185$) with standard deviation bands. The top panel shows the overall intensity, including the auto-fluorescence background, while the bottom panel displays the baseline-corrected spectra. A prominent Raman peak near 1440 cm^{-1}, corresponding to CH_2/CH_3 deformations, showed a clear intensity difference between tumor and normal tissue, enabling reliable discrimination. Highlighted region indicates the spectral window of interest for lipid/protein contrast.

As shown in Figure 5.3, in brain tissue samples, the auto fluorescence background varied more smoothly and non-linearly over the spectral range. Therefore, we needed to test multiple methods, to find the method with the highest performance on brain data.

1. Global linear interpolation: A first method estimate the baseline at 1440 cm^{-1} by linearly interpolating intensities between the two filters at (1407 cm^{-1} and 1490 cm^{-1}):

$$\hat{I}_{1440} = w_0 I_{1407} + w_1 I_{1490}, \qquad w_0 = \frac{1490 - 1440}{1490 - 1407}, \quad w_1 = \frac{1440 - 1407}{1490 - 1407}. \tag{5.1}$$

This method assumes a spatially constant fluorescence slope and in result, it left a residual wavy patterns in regions where auto fluorescence varied across the tissue.

2. Polynomial Fit: I also tested a quadratic fit to estimate the baseline using the three reference bands at 1407, 1462, and 1490 cm^{-1}:

$$I_{1440,\text{baseline}} = a \cdot (1440)^2 + b \cdot 1440 + c \tag{5.2}$$

where the coefficients a, b, and c were estimated pixel-wise using a second-order polynomial fit across the three reference bands. To model the smooth, non-linear auto fluorescence/baseline present in brain tissue Raman spectra, a pixel-wise polynomial fitting approach using `polyfit(x, y, n)`, a built-in function in MATLAB was used. This function fits a polynomial of degree n to the data points (x, y) using a least-squares approach. In our case, x represents the Raman shifts (1407, 1462, and 1490 cm^{-1}), and y is the intensity at each pixel location for the corresponding bands. We used $n = 2$ to fit a second-order (quadratic) polynomial to capture the curvature of the background. This fitting was performed independently for each image pixel. The resulting polynomial coefficients $[a, b, c]$ were then evaluated at 1440 cm^{-1} using the `polyval` function to estimate the baseline at the target band:

$$p = \texttt{polyfit}([1407, 1462, 1490], [I_{1407}, I_{1462}, I_{1490}], 2) \tag{5.3}$$

$$I_{1440,\text{baseline}} = \texttt{polyval}(p, 1440) \tag{5.4}$$

The baseline image was then subtracted from the corrected 1440 cm^{-1} image to isolate the Raman contribution.

3. Log-domain local affine baseline (final method): To handle both additive and multiplicative components, we worked in the log domain and fit a local logarithmic baseline across bands within a $w \times w$ neighborhood.

$$\log I_{\tilde{\nu}}(x, y) = a(x, y)\,(\tilde{\nu} - \bar{\nu}) + b(x, y) + r(x, y, \tilde{\nu}), \tag{5.5}$$

Where $a(x, y)$ and $b(x, y)$ are estimated by least squares over the three bands using neighborhood averages.

$$C_{1440}(x, y) = \log I_{1440}(x, y) - \Big[a(x, y)(1440 - \bar{\nu}) + b(x, y)\Big], \tag{5.6}$$

The residual at 1440 cm^{-1}, represents the Raman contrast free of both fluorescence curvature and illumination shading. This *log-local* model consistently removed the smooth background without distorting fine structural information. I choose window size w empirically and based on the final visual performance. Larger windows ($w > 25$) under-fit local baseline curvature

(leaving residual bands), while smaller windows ($w < 17$) amplify pixel noise. A value of $w = 21$ provided the best compromise, corresponding to a spatial scale roughly half the wavelength of the residual background drift observed in FFT analysis. Figure 5.4 shows the results of applying these different method on the same sample. As shown, the proposed log-domain local affine method (panel C) effectively removed the smooth auto fluorescence background and eliminated the residual wavy artifacts observed in previous approaches.

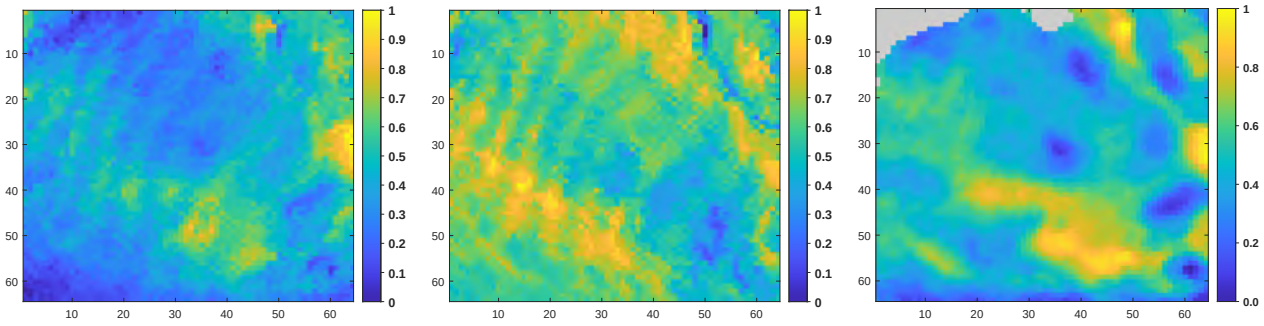

(a) Linear interpolation (b) Polynomial Fit (c) Log-local affine method

Figure 5.4 Comparison of baseline subtraction approaches at 1440 cm^{-1}.

Masking and visualization

A reference reflectance image (NaN pixels outside the tissue) defines the mask $M(x, y)$.

$$M(x,y) = \begin{cases} 1, & \text{if finite}(I_{\text{ref}}(x,y)), \\ 0, & \text{otherwise.} \end{cases} \tag{5.7}$$

All contrast maps were multiplied by M; non-tissue pixels are shown as neutral gray for visualization (Figure 5.6).

5.4.1 ROC Analysis Using Probe Data

To estimate the potential classification performance of the multi spectral Raman imaging approach, a Receiver Operating Characteristic (ROC) analysis was computed using the data acquired by prob from another study by Leblond's group [17]. In this study, the intraoperative use of the Sentry Raman spectroscopy System was tested on 67 adult patients undergoing open brain surgery at the Montreal Neurological Institute-Hospital (MNI-H, Montreal, Canada) and Mount Sinai Hospital (MSH, New York, USA). The study included patients

with glioblastoma, metastatic cancer, and meningioma. In this study, an average of 30 spectra were acquired during each acquisition. To calculate ROC based on these data, for each probe measurement, the Raman intensity was integrated across the filter bandwidth centered at the selected spectral band, indicating an area-under-curve (AUC) value that shows the filter-transmitted spectral intensity. The ROC curve was then computed by varying the classification threshold over all AUC values. The ROC analysis showed an AUC = 0.94, indicating reliable separation between normal and glioblastoma spectra at 1440 cm^{-1}. The probability that a randomly chosen normal spectrum has a higher band intensity than a randomly chosen glioblastoma spectrum is 94%. So, the filter-based method to detect the 1440 cm^{-1} provides a robust normal-tumor discrimination detection.

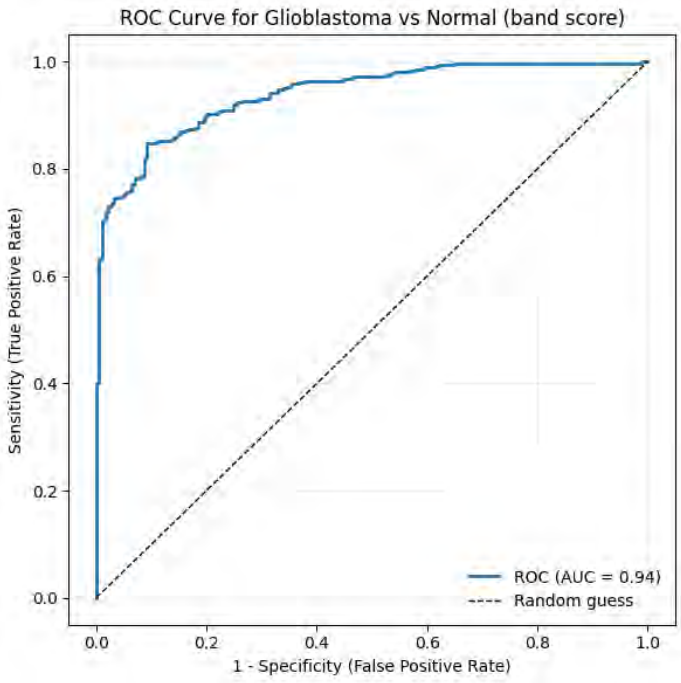

Figure 5.5 ROC curve for classification between glioblastoma and normal brain tissue based on probe-acquired Raman spectra.

5.5 Preliminary Clinical Results

To evaluate the performance of the multi-spectral Raman imaging system on clinical tissue, we present preliminary results obtained from six ex vivo samples collected from four patients. Each sample was imaged using the full Raman acquisition workflow, followed by histopathology staining for spatial validation. Figure 5.6 illustrate the imaging results for all samples. For each sample, three type of data are included; the annotated histology H&E result, showing different sample regions by a neuro pathologist, the corresponding bright-field image as a reference for orientation, and the Raman intensity map at 1440 cm^{-1}. While wide-field Raman imaging at 1440 cm^{-1} revealed spatial variations in signal intensity across brain tissue samples, direct correlation with histopathology tumor margins can not achieved in this study. Because, the observed contrast is largely dominated by optical effects present in wide-field imaging, including variations in scattering properties and surface morphology, rather than solely reflecting biochemical differences between tumor and normal tissue. Therefore, the current results do not support a definitive association between 1440 cm^{-1} intensity variations and histological cancer labels. Future studies incorporating improved scattering compensation, multi modal contrast, and larger datasets are required to disentangle optical artifacts from true molecular signatures.

Table 5.1 Summary of analyzed brain tissue samples used for Raman baseline removal evaluation. Each sample corresponds to a distinct histological case and figure reference in the Results section.

Sample ID	**Cancer Type**	**Histology Figure ID**
P02_WF1	Meningioma Grade II	A1 in Fig. 5.6
P02_WF2	Meningioma Grade II	B1 in Fig. 5.6
P07_WF1	Glioblastoma Grade IV	C1 in Fig. 5.6
P07_WF2	Glioblastoma Grade IV	D1 in Fig. 5.6
P08_WF1	Glioblastoma Grade IV	E1 in Fig. 5.6
P09_WF1	Glioblastoma Grade IV	F1 in Fig. 5.6

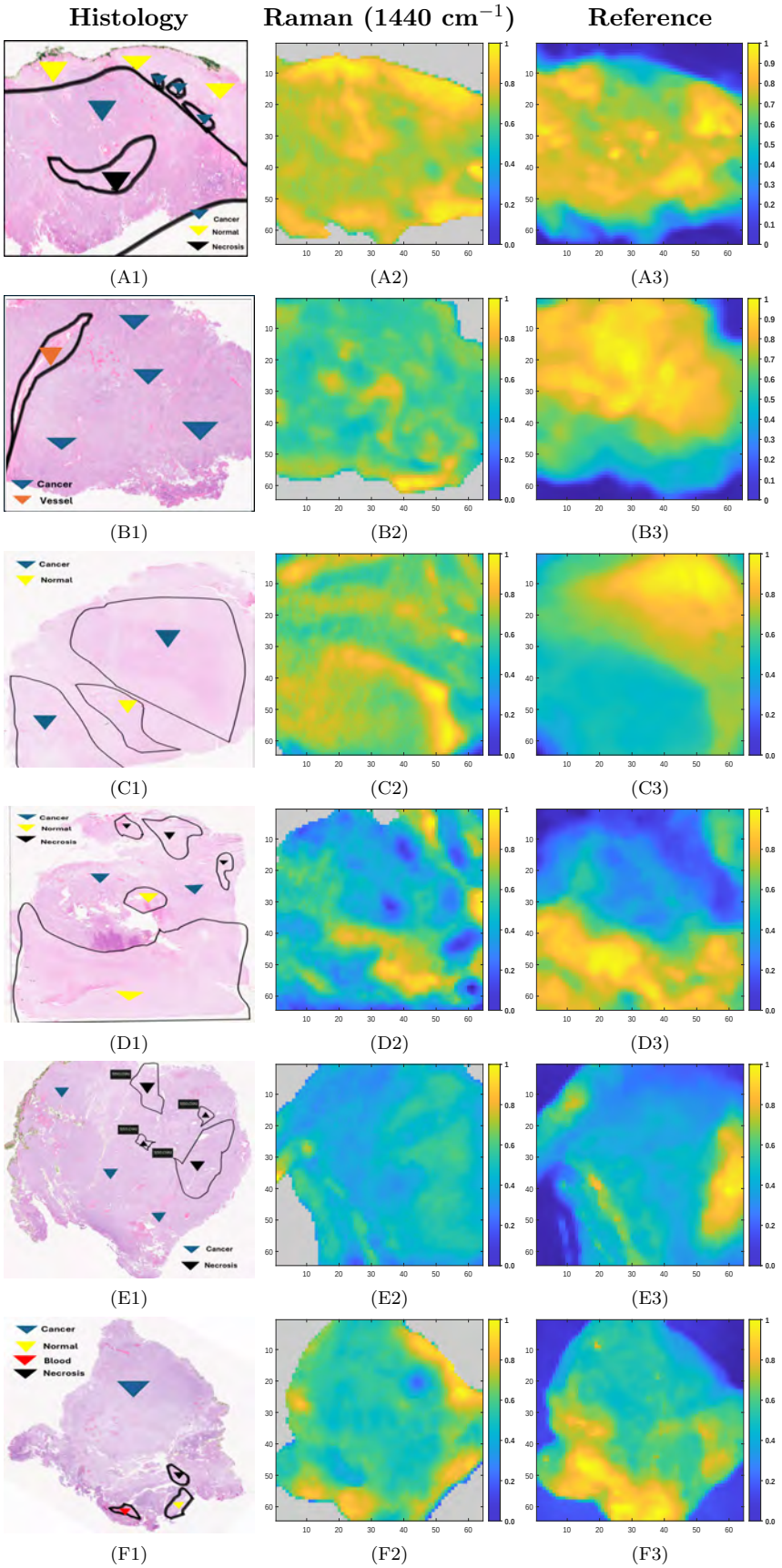

Figure 5.6 Comparison of histology(first column), Raman (second column), and reference images (third column) for six samples.

5.6 Discussion

To understand better what and how it affects the Raman intensity (attenuate or increase), we model each narrow band Raman image at Stokes wavelength λ_s as:

$$I(\lambda_s, \mathbf{r}) \;=\; S_{\text{chem}}(\Delta\nu, \mathbf{r}) \;\times\; T(\lambda_s, \mathbf{r}), \tag{5.8}$$

where S_{chem} is the intrinsic band strength (biochemistry) and T is a multiplicative throughput capturing illumination/collection and tissue transport [50]. In brain, $\mu_s'(\lambda)$ decreases gently with wavelength following a power law $\mu_s'(\lambda) = a(\lambda/500\text{ nm})^{-b}$ with $b \sim 0.7$–1.5, and is higher in white than in gray matter; tumors typically lie between them [50, 51]. For 785 nm excitation, the 1407/1440/1490 cm^{-1} bands map to ∼882.5/885.1/889.0 nm; across this 6.5 nm span, the wavelength dependence of T changes by only ∼0.6–1.2% . So in this window, scattering is a common multiplicative factor across the three bands.
Large fields often contain infiltration, necrosis/edema, and thin blood films that change μ_s' and μ_a. As a result, raw I_{1440} may show: (i) multiplicative field shading (higher $\mu_s' \Rightarrow$ brighter I_{1440}), (ii) depth weighting (higher μ_s' biases sampling toward superficial layers; necrosis/edema reduce counts), and (iii) SNR/baseline issues in areas with blood. These effects can be mitigated by reflectance normalization. This step has not been done in this thesis and would be suggested for future studies. So, in summary, I suggest the pipeline below for normalization/correction of the multi spectral Raman imaging system. Steps 1, 2, and 4 were already applied in this thesis.

5.6.1 Processing pipeline: where each correction is applied and how

Let $I_\lambda^{\text{raw}}(x, y)$ be the raw narrow band image acquired at Stokes wavelength λ (1407/1440/1490 cm^{-1} and, let $D(x, y)$ be a dark frame. All steps are applied identically to every Raman band.

(1) Dark subtraction. This step will remove camera offset and dark current:

$$\tilde{I}_\lambda = I_\lambda^{\text{raw}} - D \tag{5.9}$$

To keep the experiment conditions identical, we need to use the same exposure for D for I_λ^{raw}; median several dark to reduce read noise.

(2) System flat-field with Spectralon . We need to acquire a Spectralon image $S_\lambda(x, y)$ (same NA/focus/exposure as tissue), and then compute

$$G_\lambda(x,y) = \frac{\text{median}_{x,y}\{S_\lambda(x,y)\}}{S_\lambda(x,y)}, \qquad \hat{I}_\lambda = G_\lambda\, \tilde{I}_\lambda \tag{5.10}$$

This step will remove vignetting and pixel-response non uniformity and equalize band-to-band throughput.

(3) Scene-wise reflectance normalization (throughput/topography). A co-registered tissue reflectance image near the Stokes wavelengths ($\lambda \approx 885$–890 nm) needs to be acquired. To do this acquisition, we need to use either (i) an 880–890 nm LED (FWHM ∼10 nm) coupled into the epi path with the laser *off* and a detection BP ∼885/10, or (ii) a broadband lamp with the detection BP at 885 nm. The objective, field, focus, and camera settings should be kept identical for Raman acquisition, and then apply the same flat $G(x,y)$ and record R_{dark}. To suppress specular reflection and track diffuse reflectance, cross-polarization is also recommended. Then we need to form R and use Eq. (5.12) using a broadband illumination (tungsten/halogen or white LED). In broadband illumination, 885 nm needs to be selected using the detection filter (BP ∼885/10):

$$R(x,y) = G(x,y)\left[R_{\text{raw}}(x,y) - R_{\text{dark}}(x,y)\right] \tag{5.11}$$

Register and blur-match R to each Raman band, then divide to remove pixel-wise throughput/topography:

$$I^\star_\lambda(x,y) \;=\; \frac{\hat{I}_\lambda(x,y)}{R(x,y)} \tag{5.12}$$

(4) Baseline correction The same baseline model to each $I^\star_\lambda$ needs to be applied to obtain $I^{\star,\text{bc}}_\lambda$. Again with using identical parameters to prevent re-introducing artificial spectral tilt.

(5) QC masks and scaling. Mask pixels with low denominators, saturated pixels, or obvious blood pools.

Interpreting residuals and limitations. Spatial variations in cellularity and microstructure also can change both S_{chem} and the sampling depth. High cell density with reduced membrane lipid (e.g., GBM, larger nuclear fraction) can lower the 1440 signal despite more cells, whereas myelinated regions retain strong 1440 intensity at lower cell counts. Necrosis/edema

reduces SNR and can yield unstable ratios if unmasked. After the pipeline above, remaining differences with histology reflect biochemical heterogeneity and partial-volume (optical averaging) more than transport [50, 51].

Finally, due to the early stage of the clinical study, the dataset was limited; future work will (i) enlarge the cohort for statistical power, (ii) quantify agreement with ground-truth pathology region-by-region, and (iii) evaluate multivariate or machine-learning classifiers that exploit the full multi spectral information for tumor vs. non-tumor discrimination [52–54].

CHAPTER 6 DISCUSSION AND CONCLUSION

6.1 Summary of Contributions

This thesis presents the improvement, validation, and preliminary clinical application of a wide-field multi spectral Raman imaging system for intraoperative brain tumor detection.
I integrated a standalone, compact multi spectral Raman imaging system, enabling acquisition of spatially resolved Raman maps over a field of view exceeding 2 cm^2 with a spatial resolution of 350 µm. In parallel, I developed a Python-based software application with a graphical user interface (GUI) to automate image acquisition and control the motorized filter wheel, an essential component of the multi-spectral setup. Together, hardware integration and software automation fulfill **Objective 2** and **Objective 1** of this project, respectively.
To achieve **Objective 3**, I validated the system in porcine muscle and fat samples, demonstrating reliable detection of the lipid/protein band at 1440 cm^{-1}. I developed a calibration protocols for spectral and spatial correction using Spectralon and NIST standards, as well as a data processing pipeline, to enhance reproducibility and image fidelity.
In alignment with **Objective 4**, I performed clinical validation on ex vivo brain samples from patients with meningioma and glioblastoma. Raman intensity maps, with a focus on the 1440 cm^{-1} band associated with lipid and protein content, were produced and correlated with annotated histopathology to assess the system's ability to detect relevant biochemical features. As part of the data processing pipeline, a new baseline subtraction technique was implemented to improve the spectral accuracy and reduce the auto fluorescence background. In addition, a standardized protocol for sample preparation and spatial registration was developed to ensure precise alignment between the Raman images and histological ground truth, enabling reliable comparison and interpretation.

6.2 Advantages of the Proposed Technology

The wide-field multi spectral Raman imaging system offers several advantages over existing intraoperative guidance technologies for brain tumor surgery. Unlike fluorescence-guided techniques that require exogenous agents such as 5-ALA, this system utilizes intrinsic Raman scattering to reveal the biochemical signatures of tissues. This eliminates concerns related to patient safety, variability in drug uptake and regulatory restrictions. In the system, acquiring Raman intensity maps over a large field of view (exceeding 2 cm^2) with sub-millimeter spatial resolution allows for a comprehensive assessment of tumor margins rather than relying on

limited point measurements. Moreover, the system can target diagnostically relevant Raman bands (e.g., 1004, 1340, and 1440 cm^{-1}), enabling the detection of molecular markers related to protein, lipid, and amino acid content. This spectral flexibility allows for adaptation to various tumor types.

The use of band pass filters and simplified spectral acquisition reduces the data collection time and computational complexity. When combined with baseline correction techniques, this paves the way for real-time or near-real-time analyses during surgery.

Finally, compared to high-end intraoperative MRI, the multi spectral Raman system offers a lower-cost and easier-to-operate solution without sacrificing molecular specificity. These advantages position the developed system as a promising candidate for future clinical translation, particularly in neurosurgical settings, where precise label-free tissue characterization is critical.

6.3 Technical and Clinical Limitations

Despite promising results, several limitations were encountered,that point to future work .

Limitation in Precise Alignment : Precise comparison between the histology results and the multi-spectral Raman Imaging, needs sub-millimeter alignment. This would enable pixel-wise mapping of Raman images with corresponding areas on histological images, allowing measurement of system accuracy in detecting cancer and non-cancer areas.

Tissues Heterogeneity Effect: Tissue heterogeneity within the spatial sampling volume affect the Raman signal. The wide-field system acquires Raman spectra from areas that may contain a mixture of tumor and normal brain tissues. Because the Raman intensity at the CH_2/CH_3 deformation band is proportional to the lipid content, mixed pixels yield intermediate intensity values, reducing the contrast between cancerous and non-cancerous regions. This effect is particularly pronounced near the tumor margins, where histological annotations may still include significant fractions of normal tissue. Consequently, partial volume effects can reduce the classification accuracy and should be considered when interpreting the results. Future studies could address this by incorporating higher spatial resolution imaging or spectral un mixing methods to de-convolve mixed tissue contributions.

Depth Sensitivity of Raman Signal Collection: A key limitation of the current multi spectral Raman imaging system is the shallow sampling depth inherent to the epi-illumination geometries at 785 nm in brain tissue. Owing to the combined effects of tissue scattering and absorption, most detected Raman photons originate from the superficial layers, typically within the first 200–400 µm of the tissue surface, with rapid signal attenuation beyond 500 µm [55, 56]. Contributions from depths greater than 1 mm were negligible under these con-

ditions. Consequently, the system is primarily sensitive to biochemical variations in the surface and cannot reliably detect subsurface tumor infiltration located deeper within the parenchyma of the organ. This depth limitation should be considered when interpreting classification maps and correlating Raman findings with histopathology, particularly in cases where residual tumor tissue may be located below the accessible optical sampling depth of the tissue. Future studies could address this by exploring spatially offset Raman spectroscopy (SORS) or other photon migration–based approaches that extend the probing depth.
Auto fluorescence Interference: Brain tissue exhibits strong auto fluorescence, requiring robust baseline correction and reducing signal-to-noise ratio in some regions.
Small Clinical Sample Size: Due to early-stage clinical access, only a limited number of ex vivo samples were analyzed, restricting statistical power.

6.4 Future Studies Direction

6.4.1 Targeting 1004, 1340, and 1430–1460 cm^{-1} Bands:

Future implementations should include dedicated narrow band filters to isolate specific molecular bands such as phenylalanine (1004 cm^{-1}), tryptophan/collagen (1340 cm^{-1}), and CH_2/CH_3 deformation modes (1430–1460 cm^{-1}). Acquiring these bands individually with high spectral fidelity could improve the detection power of the multi spectral system.

6.4.2 Precise alignment of Histology and Raman Images and measuring accuracy:

I would suggest the following alignment workflow for future studies.

1. **Capture a reference image:** capture a white-light image from the same field of view of each Raman acquisition, . This image keeps the same geometry as the Raman data and will later help to map the histology section.

2. **Pre-process all images:** Raman images can be corrected for dark current, illumination, and system response using a NIST reference material (e.g., SRM 2241) [23]. Histology slides (NDPI) can be down sampled for faster processing, while keeping the pixel-to-micrometer scale. White-light images should be normalized for illumination.

3. **Align Raman to White-Light:** Because both are from the same setup, this alignment can be done simply using threshold masking, as demonstrated in this thesis for

brain tissue samples. By using the White-Light image as reference, it becomes possible to clearly identify the borders and contours of the specimen. A suitable threshold-based mask can then be applied around the tissue to preserve its spatial boundaries and to ensure that only the relevant sample area is analyzed. This approach allows the Raman data to retain its correct spatial identification while also reducing background contributions, providing a simple registration methods.

4. **Align Histology to White-Light:** The histology images often deform during slicing and staining, so a two-step approach is better: first a global alignment (affine or homograph), followed by a local non-rigid adjustment using a B-spline or thin-plate-spline model [57, 58].

5. **Combine the two transforms:** The final mapping from histology to Raman space can be expressed as:

$$T_{\text{histology}\to\text{Raman}} = T^{-1}_{\text{Raman}\to\text{WL}} \circ T_{\text{histology}\to\text{WL}} \tag{6.1}$$

   Applying this combined transform to the histology mask will bring the annotated tumor and normal regions into the Raman image space.

6. **Evaluate alignment and accuracy:** The quality of registration can be checked visually by overlaying tissue contours, and numerically using the landmark root-mean-square error (RMSE). Once aligned, the Raman intensity or classification values can be compared with histology labels to calculate metrics such as sensitivity, specificity, and area under the ROC curve (AUC).

6.4.3 Real-time Raman Classification:

Integrating real-time spectral processing and machine learning-based classification pipelines would allow instant feedback during acquisitions. This would include dedicating software to automate all the acquisition and processing steps, as well as optimizing the exposure time and laser power.

6.4.4 Multi modal Integration:

Combining wide-field Raman imaging with co-registered modalities such as white-light reflectance, intraoperative fluorescence, or optical coherence tomography could enhance tumor

delineation and compensate for individual modality limitations.

6.4.5 Power Analysis and Sample Size:

To draw statistically rigorous conclusions about system performance for cancer detection with *wide-field, multi-band* Raman imaging, needs to planned an *a priori* power analysis (G*Power [59]) should be performed using the **region/specimen** as the unit of analysis (not individual pixels). Because the specific optic design, SNR, and pre processing differ from single-point probes, a short pilot to estimate the effect size (Cohen's d) and the inter class correlation (ICC, ρ) on the multi spectral system. As an initial prior grounded in the Raman literature, we assumed a *moderate* effect size $d = 0.5$ for contrasts at 1004 and 1440 cm^{-1} [17]. With $\alpha = 0.05$ and power $1-\beta = 0.95$, a two-sample t-test requires approximately 100 independent region-level observations for each class. Wide-field imaging yields multiple correlated measurements per specimen, so we correct for clustering using the *design effect*

$$\mathrm{DE} \;=\; 1 + (m-1)\rho, \tag{6.2}$$

where m is the average number of regions per specimen, and ρ is the ICC. The total number of regions to acquire per class is then

$$N_{\mathrm{target}} \;=\; \frac{\mathrm{DE} \;\times\; n_{\mathrm{eff}}}{(1 - r_{\mathrm{QC}})}, \tag{6.3}$$

where r_{QC} accounts for quality control exclusions (e.g., QF thresholds). Based on prior clinical Raman work, we anticipate $r_{\mathrm{QC}} \approx 0.20$–$0.30$ [17]. As a concrete example, with $m = 4$ regions/specimen and $\rho = 0.3$ (DE = 1.9) and $r_{\mathrm{QC}} = 0.25$, we would plan for $N_{\mathrm{target}} \approx \frac{1.9 \times 100}{0.75} \approx 253$ regions per class. These targets will be refined after the pilot study, which will provide system-specific estimates of d and ρ.

In parallel, for classifier reporting we will size the dataset to achieve precise ROC estimates (aiming for a 95% CI width ≤ 0.10 around AUC), and we will use *patient-wise* splits (no patient overlap between train/test) to ensure generalization. Finally, because multi-band models (e.g., 1004/1340/1430–1460cm^{-1}) often yield a larger effective d than a single band, the required sample size may decrease once pilot estimates are available.

6.4.6 Ex vivo Validation Only:

Imaging was performed on ex vivo tissue; the system's performance under in vivo surgical conditions remains to be demonstrated.

REFERENCES

[1] "Fact sheet."

[2] I. D. Nagtegaal, C. A. M. Marijnen, E. K. Kranenbarg, C. J. H. van de Velde, and J. H. J. M. van Krieken, "Circumferential margin involvement is still an important predictor of local recurrence in rectal carcinoma: not one millimeter but two millimeters is the limit," *The American Journal of Surgical Pathology*, vol. 26, no. 3, pp. 350–357, 2002.

[3] R. H. Spiro, O. Guillamondegui, A. F. Paulino, and A. G. Huvos, "The pattern of invasion and margin assessment in patients with oral tongue cancer," *Head & Neck*, vol. 21, no. 5, pp. 408–413, 1999.

[4] P. I. Karakiewicz, J. A. Eastham, M. Graefen, I. Cagiannos, P. Stricker, E. Klein, T. Cangiano, F. H. Schroder, P. T. Scardino, and M. W. Kattan, "Prognostic impact of positive surgical margins in surgically treated prostate cancer: multi-institutional assessment of 5831 patients," *Urology*, vol. 66, no. 6, pp. 1245–1250, 2005.

[5] L. Qiu, D. K. Pleskow, K. Alavi, K. Itani, R. Chuttani, E. Vitkin, L. Guo, S. Kabani, N. Ozden, S. Michael, I. Itzkan, L. T. Perelman, I. J. Bigio, M. S. Feld, V. Backman, and L. T. Perelman, "Multispectral scanning during endoscopy guides the biopsy of dysplasia in barrett's esophagus," *Nature Medicine*, vol. 16, no. 5, pp. 603–606, 2010.

[6] G. M. van Dam, G. Themelis, L. M. A. Crane, N. J. Harlaar, R. G. Pleijhuis, W. Kelder, A. Sarantopoulos, J. S. de Jong, H. J. G. Arts, A. G. J. van der Zee, J. Bart, P. S. Low, and V. Ntziachristos, "Intraoperative tumor-specific fluorescence imaging in ovarian cancer by folate receptor-alpha targeting: first in-human results," *Nature Medicine*, vol. 17, no. 10, pp. 1315–1319, 2011.

[7] M. A. Whitney, J. L. Crisp, L. T. Nguyen, B. Friedman, L. A. Gross, P. Steinbach, and R. Y. Tsien, "Fluorescent peptides highlight peripheral nerves during surgery in mice," *Nature Biotechnology*, vol. 29, no. 4, pp. 352–356, 2011.

[8] H. Yoo, P. Kim, H. Lee, C. M. Castro, A. J. Hart, R. Connelley, H. Wu, and S. H. Yun, "Intra-arterial catheter for simultaneous microstructural and molecular imaging in vivo," *Nature Medicine*, vol. 17, no. 12, pp. 1680–1684, 2011.

[9] M. Diem, A. Mazur, K. Lenau, J. Schubert, B. Bird, M. Miljković, C. Krafft, and J. Popp, "Molecular pathology via ir and raman spectral imaging," *Journal of Biophotonics*, vol. 6, no. 11-12, pp. 855–886, 2013.

[10] K. Hanna, E. Krzoska, A. M. Shaaban, D. Muirhead, and AbuEid.

[11] "Image-guided raman spectroscopy navigation system to improve transperineal prostate cancer detection. part 1: Raman spectroscopy fiber-optics system and in situ tissue characterization," vol. 27. [Online]. Available: https://www.spiedigitallibrary.org/journals/journal-of-biomedical-optics/volume-27/issue-9/095003/Image-guided-Raman-spectroscopy-navigation-system-to-improve-transperineal-prostate/10.1117/1.JBO.27.9.095003.full

[12] S. David, T. Tran, F. Dallaire, G. Sheehy, F. Azzi, D. Trudel, F. Tremblay, A. Omeroglu, F. Leblond, and S. Meterissian, "In situ raman spectroscopy and machine learning unveil biomolecular alterations in invasive breast cancer," *J Biomed Opt*, vol. 28.

[13] G. Sheehy, F. Picot, F. Dallaire, K. J. Ember, T. Nguyen, K. Petrecca, D. Trudel, and F. Leblond, "Open-sourced raman spectroscopy data processing package implementing a baseline removal algorithm validated from multiple datasets acquired in human tissue and biofluids," vol. 28, no. 2, p. 025002, publisher: SPIE. [Online]. Available: https://www.spiedigitallibrary.org/journals/journal-of-biomedical-optics/volume-28/issue-2/025002/Open-sourced-Raman-spectroscopy-data-processing-package-implementing-a-baseline/10.1117/1.JBO.28.2.025002.full

[14] F. Daoust, H. Tavera, F. Dallaire, P. Orsini, K. Savard, J. Bismuth, P. Mckoy, I. Veilleux, K. Petrecca, and F. Leblond, "A clinical raman spectroscopy imaging system and safety requirements for *in situ* intraoperative tissue characterization," vol. 148, no. 9, pp. 1991–2001. [Online]. Available: http://xlink.rsc.org/?DOI=D2AN01946A

[15] F. Daoust, T. Nguyen, P. Orsini, J. Bismuth, M.-M. d. Denus-Baillargeon, I. Veilleux, A. Wetter, P. McKoy, I. Dicaire, M. Massabki, K. Petrecca, and F. Leblond, "Handheld macroscopic raman spectroscopy imaging instrument for machine-learning-based molecular tissue margins characterization," *JBO*, vol. 26, no. 2, p. 022911, publisher: SPIE. [Online]. Available: https://www.spiedigitallibrary.org/journals/journal-of-biomedical-optics/volume-26/issue-2/022911/Handheld-macroscopic-Raman-spectroscopy-imaging-instrument-for-machine-learning-based/10.1117/1.JBO.26.2.022911.full

[16] K. St-Arnaud, K. Aubertin, M. Strupler, W.-J. Madore, A.-A. Grosset, K. Petrecca, D. Trudel, and F. Leblond, "Development and characterization of a handheld hyperspectral raman imaging probe system for molecular characterization of tissue on mesoscopic scales," *Medical Physics*, vol. 45, no. 1, pp. 328–339, _eprint: https://onlinelibrary.wiley.com/doi/pdf/10.1002/mp.12657. [Online]. Available: https://onlinelibrary.wiley.com/doi/abs/10.1002/mp.12657

[17] K. Ember, F. Dallaire, A. Plante, G. Sheehy, M.-C. Guiot, R. Agarwal, R. Yadav, A. Douet, J. Selb, J. P. Tremblay *et al.*, "In situ brain tumor detection using a raman spectroscopy system—results of a multicenter study," *Scientific Reports*, vol. 14, no. 1, p. 13309, 2024.

[18] B. Sommer, P. Grummich, H. Hamer, I. Bluemcke, R. Coras, M. Buchfelder, and K. Roessler, "Frameless stereotactic functional neuronavigation combined with intraoperative magnetic resonance imaging as a strategy in highly eloquent located tumors causing epilepsy," *Stereotactic and Functional Neurosurgery*, vol. 92, no. 1, pp. 59–67, 2014.

[19] P. Charalampaki, P. J. Proskynitopoulos, A. Heimann, and M. Nakamura, "5-aminolevulinic acid multispectral imaging for the fluorescence-guided resection of brain tumors: A prospective observational study," *Frontiers in Oncology*, vol. 10, p. 1069, 2020.

[20] C. de Quintana-Schmidt, L. Salgado-Lopez, J. A. Aibar-Duran, M. J. Alvarez Holzapfel, C. A. Cortes, J. D. P. Alvarado, R. R. Rodriguez, and J. M. Teixidó, "Neuronavigated ultrasound in neuro-oncology: A true real-time intraoperative image," *World Neurosurgery*, vol. 157, pp. e316–e326, 2022. [Online]. Available: https://www.sciencedirect.com/science/article/pii/S1878875021015795

[21] J. Mito, J. Ferrer, C.-L. Lee, R. Dodd, W. Eward, L. Marshall, K. Cuneo, J. Carter, S. Ramasunder, Y. Kim, W. D. Lee, L. Griffith, R. Bouzaiene, and D. Kirsch, "Intraoperative detection and removal of microscopic residual sarcoma using wide-field imaging," *Cancer*, vol. 118, pp. 5320–30, 11 2012.

[22] W. contributors, "Raman spectroscopy: Energy levels diagram," https://en.wikipedia.org/wiki/Raman_spectroscopy#/media/File:Raman_energy_levels.svg, 2024, accessed: November 22, 2024.

[23] F. Daoust, "Large field of view raman imaging clinical prototype to guide brain cancer resection surgery," Ph.D. thesis, Polytechnique Montréal, Montréal, QC, Canada, 2024, available at PolyPublie. [Online]. Available: https://publications.polymtl.ca/58355/

[24] M. Jermyn, K. W. Mok, J. Mercier, J. Desroches, J. Pichette, K. Saint-Arnaud, M.-C. Guiot, E. Marple, K. Petrecca, and F. Leblond, "Intraoperative brain cancer detection with raman spectroscopy in humans," *Science Translational Medicine*, vol. 7, no. 274, p. 274ra19, 2015. [Online]. Available: https://www.science.org/doi/10.1126/scitranslmed.aaa2384

[25] S. e. a. David, "Towards non-contact macroscopic imaging of multiple cancers using multi-spectral inelastic scattering detection," *(In review)*, 2024.

[26] F. e. a. Ringel, "Clinical benefit from resection of recurrent glioblastomas: results of a multicenter study including 503 patients," *Neuro-oncology*, vol. 18, no. 1, pp. 96–103, 2016.

[27] A. Wu, J. Rees, and M. Greaves, "Glioblastoma multiforme: A review of where we have been and where we are going," *Expert Review of Anticancer Therapy*, vol. 21, no. 3, pp. 305–317, 2021.

[28] M. e. a. Diem, "Molecular pathology via ir and raman spectral imaging," *Journal of Biophotonics*, vol. 6, no. 11-12, pp. 855–886, 2013.

[29] H. e. a. Yoo, "Intra-arterial catheter for simultaneous microstructural and molecular imaging in vivo," *Nature Medicine*, vol. 17, no. 12, pp. 1680–1684, 2011.

[30] W. e. a. Stummer, "Fluorescence-guided surgery with 5-ala for resection of malignant glioma: a randomized controlled multicentre phase iii trial," *The Lancet Oncology*, vol. 7, no. 5, pp. 392–401, 2011.

[31] W. Stummer, U. Pichlmeier, T. Meinel, O. D. Wiestler, F. Zanella, H.-J. Reulen, and ALA-Glioma Study Group, "Fluorescence-guided surgery with 5-aminolevulinic acid for resection of malignant glioma: a randomised controlled multicentre phase III trial," vol. 7, no. 5, pp. 392–401.

[32] G. e. a. van Dam, "Intraoperative tumor-specific fluorescence imaging in ovarian cancer by folate receptor-alpha targeting," *Nature medicine*, vol. 17, no. 10, pp. 1315–1319, 2011.

[33] G. Keiser, *Optical Fiber Communications*, 4th ed. Springer, 2016.

[34] S. L. Jacques, "Optical properties of biological tissues: a review," *Physics in Medicine & Biology*, vol. 58, no. 11, pp. R37–R61, 2013.

[35] J. A. Kim, D. J. Wales, and G.-Z. Yang, "Optical spectroscopy for *in vivo* medical diagnosis—a review of the state of the art and future perspectives," vol. 2, no. 4, p. 042001. [Online]. Available: https://iopscience.iop.org/article/10.1088/2516-1091/abaaa3

[36] J. R. Lakowicz, *Principles of fluorescence spectroscopy*, third edition, corrected at 4. printing ed. Springer.

[37] W. Demtroder, *Molecular Physics: Theoretical Principles and Experimental Methods*. Berlin, Heidelberg: Springer, 2015.

[38] B. E. A. Saleh and M. C. Teich, *Fundamentals of Photonics*, 2nd ed. Hoboken, NJ: Wiley, 2007.

[39] L. V. Wang and S. Hu, "Photoacoustic tomography: in vivo imaging from organelles to organs," *Science*, vol. 335, no. 6075, pp. 1458–1462, 2012.

[40] A. H. Akbarzadeh, D. R. Thompson, M. Lalonde, and F. Leblond, "Experimental validation of a spectroscopic monte carlo light transport simulation technique and depth sensing analysis in biological tissue," *Scientific Reports*, vol. 11, no. 1, p. 10884, 2021.

[41] F. in Oncology Contributors, "Intraoperative visualization of gliomas using raman spectroscopy," *Frontiers in Oncology*, 2022. [Online]. Available: https://www.frontiersin.org/articles/10.3389/fonc.2022.1086643/full

[42] M. Contributors, "Current applications of raman spectroscopy in neurosurgical guidance," *Cancers*, 2023. [Online]. Available: https://www.mdpi.com/2227-9059/12/10/2363

[43] Innovative Photonic Solutions, "3/5/7 UP 785 nm Spectrum Stabilized Laser Module Specifications," https://www.ipslasers.com, 2023.

[44] Finger Lakes Instrumentation, LLC, "High Speed Filter Wheel User's Guide," https://www.flicamera.com, 2018, revision June 2018.

[45] J. R. Lakowicz, *Principles of Fluorescence Spectroscopy*, 3rd ed. Springer, 2006.

[46] Andor Technology Ltd., "iKon-M 934 CCD Camera Specifications," https://andor.oxinst.com/products/ikon-m-ccd-camera/ikon-m-934, 2023, document No. DU934P-xxxx, Rev. 0523 R1.

[47] A. Vogel and V. Venugopalan, "Mechanisms of laser-induced thermal tissue damage," *Chemical Reviews*, vol. 103, no. 2, pp. 577–644, 2003.

[48] M. H. Niemz, *Laser-Tissue Interactions: Fundamentals and Applications*, 3rd ed. Springer, 2007.

[49] Laser Institute of America, "American national standard for safe use of lasers (ansi z136.1)," 2020, orlando, FL: LIA.

[50] S. L. Jacques, "Optical properties of biological tissues: a review," *Physics in Medicine & Biology*, vol. 58, no. 11, pp. R37–R61, 2013.

[51] A. N. Yaroslavsky, P. C. Schulze, I. V. Yaroslavsky, R. Schober, F. Ulrich, and H. J. Schwarzmaier, "Optical properties of selected native and coagulated human brain tissues in vitro in the visible and near infrared spectral range," *Physics in Medicine and Biology*, vol. 47, no. 12, pp. 2059–2073, 2002.

[52] T. Hollon, B. Pandian, A. R. Adapa, E. Urias, A. V. Save, S. S. Khalsa, D. G. Eichberg, R. S. D'Amico, Z. U. Farooq, S. Lewis, J. Xiang, O. Sagher, L. A. Snyder, S. E. Sullivan, E. L. McKean, E. George, K. Hoversten, P. A. Valdes, J. Smith, and D. A. Orringer, "Near real-time intraoperative brain tumor diagnosis using stimulated raman histology and deep neural networks," *Nature Medicine*, vol. 26, pp. 52–58, 2020.

[53] A. Beljebbar, D. Bouchon, S. Koljenović, G. J. Puppels, F. Argoul, and M. Manfait, "Identification of raman spectroscopic markers for histopathology: towards spectral histopathology," *Journal of Raman Spectroscopy*, vol. 41, no. 12, pp. 1529–1537, 2010.

[54] M. Ji, S. Lewis, S. Camelo-Piragua, S. Ramkissoon, M. Snuderl, S. Venneti, A. Fisher-Hubbard, M. Garrard, D. Fu, A. C. Wang, J. A. Heth, J. Oertel, O. Sagher, Y. Xiao, N. Sanai, T. D. Johnson, C. W. Freudiger, G. S. Young, J. T. C. Liu, A. I. Mehta, P. Mukherjee, K. M. Muraszko, S. H. Ramkissoon, M. Snuderl, S. Santagata, D. A. Orringer, and X. S. Xie, "Rapid, label-free detection of brain tumors with stimulated raman scattering microscopy," *Science Translational Medicine*, vol. 5, no. 201, p. 201ra119, 2013.

[55] O. R. Scepanovic, Z. Volynskaya, C. R. Kong, R. R. Dasari, M. Fitzmaurice, and M. S. Feld, "Depth profiling with confocal raman microspectroscopy," *Applied Optics*, vol. 46, no. 10, pp. 1911–1917, 2007.

[56] P. Matousek and N. Stone, "Development of deep subsurface raman spectroscopy for medical diagnosis and disease monitoring," *Chemical Society Reviews*, vol. 45, no. 7, pp. 1794–1802, 2016.

[57] S. Klein, M. Staring, K. Murphy, M. A. Viergever, and J. P. W. Pluim, "elastix: a toolbox for intensity-based medical image registration," *IEEE Transactions on Medical Imaging*, vol. 29, no. 1, pp. 196–205, 2010.

[58] Z. Yaniv, B. C. Lowekamp, H. J. Johnson, and R. Beare, "Simpleitk image-analysis notebooks: a collaborative environment for education and reproducible research," *Journal of Digital Imaging*, vol. 31, no. 3, pp. 290–303, 2018.

[59] F. Faul, E. Erdfelder, A.-G. Lang, and A. Buchner, "G*power 3: A flexible statistical power analysis program for the social, behavioral, and biomedical sciences," *Behavior Research Methods*, vol. 39, no. 2, pp. 175–191, 2007.